

UTRECHT UNIVERSITY

TOPOLOGY OF WEYL SEMIMETALS
with non-orientable Brillouin zones

by

Thijs DOUWES

A THESIS

Submitted to the Department of Physics
in partial fulfilment of the requirements
for the degree of

Master of Science

under the joint supervision of

Project supervisor

Prof. Cristiane DE MORAIS
SMITH
Department of Physics

Direct supervisor

Dr. Marcus STÅLHAMMAR
Department of Physics

October 2024

Abstract

Contents

1	Introduction	3
1.1	Main results	3
1.2	Overview	3
1.3	Prerequisites	3
1.4	Notational conventions	3
2	Topological states of matter & symmetries	4
2.1	Basic definitions	4
2.1.1	Bloch theory	4
2.2	The Su–Schrieffer–Heeger model	5
2.3	Classification of symmetries	10
2.4	Higher-dimensional models	10
2.4.1	The Chern insulator	10
2.4.2	Quantum spin Hall effect	10
2.4.3	3D strong and weak insulators	10
3	Weyl semimetals	11
3.1	Physical aspects	11
3.1.1	Weyl points	12
3.1.2	Global features	13
3.1.3	Semimetals with symmetries	14
3.2	Topological description	17
3.2.1	3D Chern insulators	17
3.2.2	Topology with Weyl points	20
3.2.3	The semimetal Mayer–Vietoris sequence	25
3.2.4	Time-reversal symmetric Weyl semimetals	28
4	Non-orientable systems	32
4.1	Review of recent literature	32
4.1.1	Non-orientable Weyl semimetals	35
4.2	Topological exploration	38
4.2.1	Preliminary clarifications	39
4.2.2	Classification scheme	42
4.2.3	Computation of invariants on $K^2 \times S^1$	46
4.3	Conclusions and outlook	52

APPENDICES

A Homology and cohomology	56
----------------------------------	-----------

Chapter 1

Introduction

1.1 Main results

1.2 Overview

1.3 Prerequisites

1.4 Notational conventions

...

Chapter 2

Topological states of matter & symmetries

Sources: [1, 2, 3, 4]

Topo phases occur in nature: [5]

Finish intro when chapter is more complete

2.1 Basic definitions

- Conducting properties of materials are understood in terms of band structure → Fermi energy. Conductance means Fermi level lies inside one of the bands. [picture]
- N -band system has hilbert space $\mathcal{H} \cong \mathbb{C}^N$, Hamiltonian represented by $N \times N$ matrix. Static system: $H\psi = E\psi$, eigenvalues are energy bands.
- Mostly interested in 2-band systems since only valence/conduction bands are relevant. Then H is a 2×2 Hermitian (for now) matrix. These are given by $H = h_0\mathbb{I} + \mathbf{h} \cdot \boldsymbol{\sigma}$ in general (h_0 changes the energy of all bands but does not affect topology of band crossings) → Bloch Hamiltonian [higher dimensional systems: Clifford algebra]
- For a Bloch Hamiltonian, eigenvalues are $\pm|\mathbf{h}|$, so conductance occurs when $\mathbf{h} = 0$.
- Insulating Hamiltonians are adiabatically connected if they can be continuously deformed into each other without band crossings. Insulators are considered topological if they are not adiabatically connected to a reference trivial phase; then these inhabit different regions of the phase diagram → existence of edge states (not always [3], footnote)

2.1.1 Bloch theory

- We work with crystalline materials which are composed of periodically repeating unit cells.

- In the bulk, we assume the Hamiltonian is periodic in the unit cell. This enables use of Bloch's theorem [6] $\psi(\mathbf{r}) = e^{i\mathbf{k}\cdot\mathbf{r}} u_{\mathbf{k}}(\mathbf{r})$.
- Different values of crystal momentum may yield identical eigenstates, the set of equivalence classes is the Brillouin zone
- Brillouin zone usually has \mathbb{T}^n topology, but internal symmetries etc. may alter this [7] [other sources]
- Discuss dispersion relations

2.2 The Su–Schrieffer–Heeger model

- SSH is usually introduced "physics first", but we would like to work backwards in a sense, to see how bulk topology gives rise to physical properties of a system.

We will take the approach of deriving the Su–Schrieffer–Heeger (SSH) model by beginning with a generic one-dimensional crystal, and introducing two topologically distinct phases in the simplest way possible.

Concretely, consider an infinite one-dimensional chain of unit cells indexed by $n \in \mathbb{Z}$; at this point, we make no assumptions on the internal structure of these unit cells. A boundary will be introduced later, but its relevant properties will turn out to be determined by the crystal's bulk topology. Suppose the real-space Hamiltonian of the system is periodic in the unit cells. By Bloch's theorem, two crystal momenta k and k' are then equivalent if they differ by an integer multiple of 2π . This means that the Brillouin zone B can be taken to be the interval $[-\pi, \pi]$, with the points $-\pi$ and π identified; this space is homeomorphic to the circle S^1 .

We might begin with a simple two-band Bloch Hamiltonian $H(k) = \mathbf{h}(k) \cdot \boldsymbol{\sigma}$, with

$$\mathbf{h} : B \cong S^1 \rightarrow \mathbb{R}^3, \quad k \mapsto \begin{pmatrix} h_x(k) \\ h_y(k) \\ h_z(k) \end{pmatrix}.$$

Such a Hamiltonian describes a gapped phase precisely when the map \mathbf{h} is non-zero everywhere, so that the topological classification of these phases is given by classes of maps from S^1 to \mathbb{R}^3 minus the origin—that is, homotopy classes of loops in $\mathbb{R}^3 \setminus \{0\}$. However, this space has a trivial fundamental group $\pi_1(\mathbb{R}^3 \setminus \{0\}) \cong 0$, meaning that all such loops can be contracted to a point; in other words, all gapped Hamiltonians are adiabatically connected, and there are no topologically interesting phases.

This situation can be remedied by imposing a constraint on the Hamiltonian: we require that $h_z(k) = 0$. Doing this effectively reduces \mathbf{h} to a two-dimensional map:

$$\mathbf{h} : B \cong S^1 \rightarrow \mathbb{R}^3, \quad k \mapsto \begin{pmatrix} h_x(k) \\ h_y(k) \end{pmatrix}.$$

The gapped phases are now classified by the non-trivial fundamental group $\pi_1(\mathbb{R}^2 \setminus \{0\}) \cong \mathbb{Z}$. This group is indexed by winding number: loops that wind around the

origin $a \in \mathbb{Z}$ times cannot be deformed into those with a different winding number $b \neq a$. In particular, loops with a non-zero winding number cannot be contracted to a point, and the associated phases are considered topological. Note that imposing a constraint on the Hamiltonian has made this system rather more interesting from a topological point of view, even though it seems like it has been simplified. Once we move to the physical picture, we will see that this restriction corresponds to imposing a certain symmetry on the system.

Let us now choose a more specific Hamiltonian to arrive at a concrete physical system. We begin with the simplest possible¹ topologically distinct states, one trivial and one topological:

$$\mathbf{h}_{\text{triv}}(k) = \begin{pmatrix} 1 \\ 0 \\ 0 \end{pmatrix}, \quad \mathbf{h}_{\text{top}}(k) = \begin{pmatrix} \cos(k) \\ \sin(k) \\ 0 \end{pmatrix}.$$

To characterise a phase transition between these two states, we consider the linear combination $\mathbf{h}(k) = v\mathbf{h}_{\text{triv}}(k) + w\mathbf{h}_{\text{top}}(k)$, with $v, w \geq 0$. The phase described by the resulting Bloch Hamiltonian is trivial when $v > w$, gapless (i.e. conducting) when $v = w$, and topological when $v < w$; see Figure 2.1.

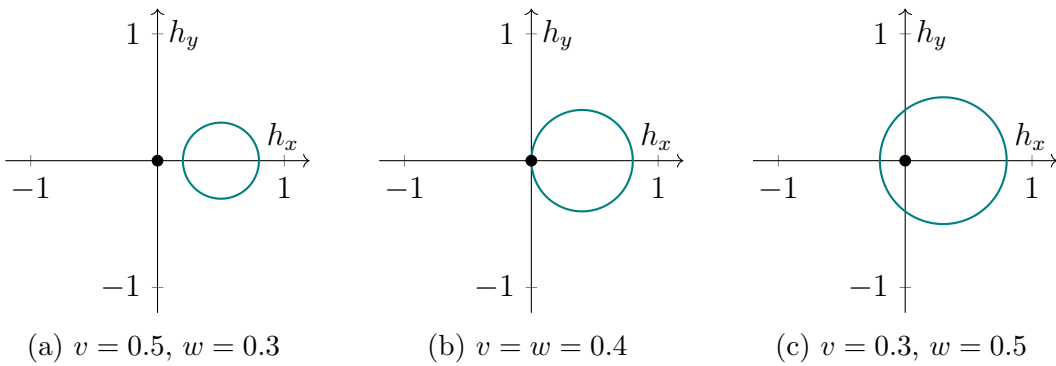


Figure 2.1: Contours in Hamiltonian space for (a) trivial, (b) conducting and (c) topological phases.

We are now in a position to start analysing the physics of the system. Concretely, the momentum space Hamiltonian is given by

$$H(k) = \mathbf{h}(k) \cdot \boldsymbol{\sigma} = (v + w \cos(k))\sigma_x + w \sin(k)\sigma_y = \begin{pmatrix} 0 & v + w e^{-ik} \\ v + w e^{ik} & 0 \end{pmatrix}.$$

We can set up a Fourier transform to real space by rewriting this suggestively in terms of the unit cell index n :

$$H(k) = e^{-ik(n-n)} \begin{pmatrix} 0 & v \\ v & 0 \end{pmatrix} + e^{-ik((n+1)-n)} \begin{pmatrix} 0 & w \\ 0 & 0 \end{pmatrix} + e^{-ik(n-(n+1))} \begin{pmatrix} 0 & 0 \\ w & 0 \end{pmatrix}$$

I need to work out the details of this Fourier transform later, my calculations aren't working out. Transforming from a periodic Brillouin zone to (discrete or infinite)

¹Our particular choice of x , y , and z coordinates very conveniently leads to the SSH model. However, mathematically speaking, all similar models are related by a simple change of basis.

real space is breaking my brain. I imagine it needs to look something like this (where $M_{0/\pm 1}$ are the three matrices above):

$$\begin{aligned}
 \hat{H} &= \int_B H(k) |k\rangle \langle k| \\
 &= \int_{-\pi}^{\pi} \frac{dk}{2\pi} \left(\sum_{a \in \{0, \pm 1\}} e^{-ika} M_a \right) \left(\sum_n e^{-ikn} |n\rangle \right) \left(\sum_{n'} \langle n'| e^{ikn'} \right) \\
 &= \sum_{a,n,n'} \left(\int_{-\pi}^{\pi} \frac{dk}{2\pi} e^{-ik(a+n-n')} \right) M_a |n\rangle \langle n'| \\
 &= \sum_{a,n,n'} \delta_{n+a,n'} M_a |n\rangle \langle n'| \\
 &= \sum_{a,n} M_a |n\rangle \langle n+a|
 \end{aligned}$$

But I don't fully understand the first step, the sign of a is wrong and normalization is broken. Maybe it's easier to discretize first and do a DFT?

- It follows [how exactly?] that we can write the Hamiltonian in a unit cell basis as

$$\hat{H} = \sum_{n=-\infty}^{\infty} \left[|n\rangle \langle n| \otimes \begin{pmatrix} 0 & v \\ v & 0 \end{pmatrix} + (|n+1\rangle \langle n| \otimes \begin{pmatrix} 0 & w \\ 0 & 0 \end{pmatrix} + \text{h.c.}) \right]$$

- Mention tight binding somewhere around this point

This Hamiltonian contains a term which acts within the unit cells, and terms which act between neighbouring unit cells, parametrized by v and w respectively. The structure of these interactions can be made somewhat more transparent by going to a finite chain of length N . The Hamiltonian then becomes

$$\hat{H} = \sum_{n=0}^N |n\rangle \langle n| \otimes \begin{pmatrix} 0 & v \\ v & 0 \end{pmatrix} + \sum_{n=0}^{N-1} \left(|n+1\rangle \langle n| \otimes \begin{pmatrix} 0 & w \\ 0 & 0 \end{pmatrix} + \text{h.c.} \right),$$

where open boundary conditions have been introduced on the ends of the chain to allow the boundary behaviour to be studied. The tensor products can be expanded in order to cast the Hamiltonian into a full $2N \times 2N$ matrix:

$$\hat{H} = \begin{pmatrix} 0 & v & 0 & 0 & & & & & \\ v & 0 & w & 0 & & & & & \\ 0 & w & 0 & v & & & & & \\ 0 & 0 & v & 0 & & & & & \\ & & & & \ddots & & & & \\ & & & & & 0 & & & \\ & & & & & & \ddots & & \\ & & & & & & & 0 & 0 \\ 0 & & & & & & & w & 0 \\ & & & & & & & 0 & w & 0 \\ & & & & & & & 0 & 0 & v \\ 0 & 0 & v & 0 & & & & 0 & 0 & 0 \end{pmatrix}.$$

A physical interpretation of this system presents itself in the form of this matrix: it describes a chain of $2N$ sites, with alternating hopping amplitudes v and w between neighbouring sites. The unit cells now consist of two of these sites, and v and w are referred to as the *intra-cell* and *inter-cell* hoppings, respectively. When these two hoppings are equal, the system is in the gapless phase $v = w$, corresponding to a chain where all bonds are equally strong. Intuitively, this homogeneity allows electrons to propagate freely along the chain. On the other hand, in the insulating cases $v \neq w$, one of the two hoppings is stronger than the other, and the electrons tend to be confined around these stronger bonds.

Dividing the unit cells into two individual sites in this way allows us to distinguish two so-called *sublattices* of the crystal, which we label A and B . The notation can then be simplified by labelling quantum states according to the sublattice on which they are localized:

$$|n, A\rangle \equiv |n\rangle \otimes \begin{pmatrix} 1 \\ 0 \end{pmatrix}, \quad |n, B\rangle \equiv |n\rangle \otimes \begin{pmatrix} 0 \\ 1 \end{pmatrix}.$$

In this notation, the Hamiltonian becomes

$$\hat{H} = \left(\sum_{n=0}^N v |n, B\rangle \langle n, A| + \sum_{n=0}^{N-1} w |n+1, A\rangle \langle n, B| \right) + \text{h.c.} \quad (2.1)$$

The tight-binding model of alternating hoppings is precisely the SSH model: it was introduced in 1979 by Wu-Pei Su, John Robert Schrieffer, and Alan J. Heeger to describe polyacetylene (Figure 2.2), a polymer chain which features alternating single and double covalent bonds [8, 9]. This material displays unexpectedly high

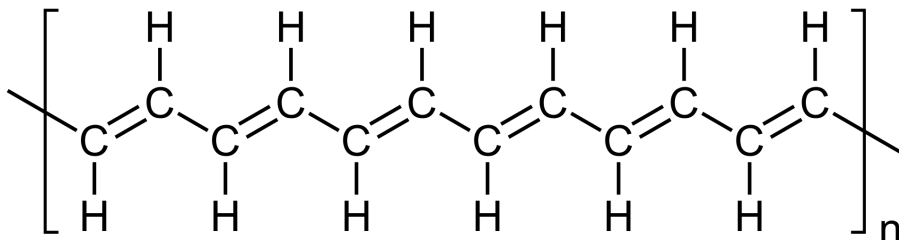


Figure 2.2: Structural diagram of polyacetylene. Electrons are transported more readily along the double bonds, which is modelled using a larger hopping parameter.

conductivity when doped with halogen impurities, and the SSH model affords an explanation for this.

To understand how this metallic behaviour comes about, the differences between the trivial and the topological phase must be examined more closely. The two phases appear to be identical at a first glance: if the unit cell in polyacetylene is chosen in such a way that the stronger double bond represents the intra-cell hopping v , then the system is in the trivial phase $v > w$, and if instead the unit cell is centred around a single bond, $v < w$ and the phase is topological. In either case, valence

electrons are expected to remain localized around the double bonds, leading to the same insulating bulk behaviour.²

The difference between the two phases only becomes apparent when the endpoints of the chain are studied. [introduce a figure here] For example, the leftmost atom is not subject to any inter-cell hopping, and it is only connected to the other atom in its unit cell. In the trivial case, this connection is strong and the two atoms share their valence electrons. In the topological phase, on the other hand, the second atom from the left prefers to share electrons with its right-hand neighbour, and the leftmost atom becomes isolated. In the limit where v goes to zero, this isolation becomes complete and the edge sites carry zero-energy eigenstates. In this case, only the second term in the Hamiltonian (2.1) survives, and the edges obey the eigenvalue equations

$$\hat{H} |1, A\rangle = \hat{H} |N, B\rangle = 0.$$

These edge modes can be shown to persist for non-zero $v < w$, in which case they become highly localized and approach zero energy in the $N \rightarrow \infty$ limit.³ The salient point is that the boundary modes of the topological phase exist inside the energy gap: their energy eigenvalues have a degeneracy at the Fermi level $\varepsilon_F = 0$. [Perhaps include dispersion figure]

Something remarkable has happened: we have started from a topological description of a gapped bulk phase, and the resulting physical effects appear as in-gap zero energy modes on the boundary of the material. As will become apparent looking at other examples, the existence of edge modes at the Fermi level is a fairly⁴ general feature of topological phases of matter, captured in the so-called *bulk-boundary correspondence*. It can be thought of as being a result of the inability to go continuously from a topological gapped phase to a trivial one in real space; in particular, the outside boundary of an idealised material connects to the vacuum, which is also considered a trivial gapped phase.

- Discuss physics of polyacetylene (solitons on trivial/topological interface) and experimental observations of solitons + berry phase [11, 12]
- We can now physically interpret the meaning of setting $h_z = 0$: it ensures that hopping only occurs between the two sublattices A and B , and not within them (i.e. there are only off-diagonal elements in the internal degrees of freedom). If we define the sublattice projection operators

$$\hat{P}_A = \mathbb{I} \otimes \begin{pmatrix} 1 & 0 \\ 0 & 0 \end{pmatrix}, \quad \hat{P}_B = \mathbb{I} \otimes \begin{pmatrix} 0 & 0 \\ 0 & 1 \end{pmatrix}$$

²The attentive reader might wonder why the conducting $v = w$ phase does not occur naturally in this system. This is a result of the so-called Peierls transition: in a nutshell, introducing a band gap locally lowers the energy of the (filled) valence band and raises that of the (empty) conduction band. This makes it energetically favourable for atoms in the chain to pair up, in a process referred to as dimerisation.

³A precise understanding of this is beyond the scope of this review; the interested reader is referred to e.g. [2].

⁴This is not a completely general statement: topological phases with edge modes at energies other than ε_F have been shown to be theoretically feasible [10]. For our purposes, it will be sufficient to restrict our attention to edge modes at the Fermi level.

then the Hamiltonian obeys

$$\hat{P}_A \hat{H} \hat{P}_A = \hat{P}_B \hat{H} \hat{P}_B = 0$$

and so since $\hat{P}_A + \hat{P}_B$ is the identity we have

$$\begin{aligned}\hat{H} &= (\hat{P}_A + \hat{P}_B) \hat{H} (\hat{P}_A + \hat{P}_B) \\ &= \hat{P}_A \hat{H} \hat{P}_B + \hat{P}_B \hat{H} \hat{P}_A \\ &= (\hat{P}_A - \hat{P}_B) \hat{H} (\hat{P}_B - \hat{P}_A) \\ &\equiv -\hat{\Gamma} \hat{H} \hat{\Gamma}\end{aligned}$$

with $\hat{\Gamma} \equiv \hat{P}_A - \hat{P}_B$ having the property that $\hat{\Gamma} = \hat{\Gamma}^{-1} = \hat{\Gamma}^\dagger$; this is called sublattice symmetry and it also applies to the momentum space Hamiltonian $H(k)$.

- An immediate consequence of our setup is that the trivial and topological phase become adiabatically connected if we allow for sublattice symmetry breaking ($h_z \neq 0$).
- Talk more about \mathbb{Z} invariant (next-nearest-neighbour hopping etc.)

2.3 Classification of symmetries

2.4 Higher-dimensional models

2.4.1 The Chern insulator

- The 2nd cohomology group introduced here classifies complex vector bundles over the Brillouin zone. The vector bundle classification point of view is not one we will pursue in detail in this work, but it is in some ways more fundamental than the description in terms of Berry curvature, especially for systems with additional symmetries. This makes it the preferred point of view for precise mathematical classification schemes.

2.4.2 Quantum spin Hall effect

- Introduce the \mathbb{Z}_2 FKMI invariant in 2D, both in terms of product-of-signs and EBZ integral. (Perhaps mention twisted equivariant cohomology? Not the classical treatment and may not be necessary at this point)

2.4.3 3D strong and weak insulators

- Refer to tenfold way, weak \mathbb{Z}_2 topology on T-invariant 2D subsystems and strong 3D \mathbb{Z}_2 invariant based both on POS and difference of weak invariants.

Chapter 3

Weyl semimetals

In recent years, interest in topological materials has expanded beyond the purely gapped phases in insulators and superconductors, into the realm of metals and other related gapless phases. Some of the topological conductors that are of the greatest interest are called Weyl semimetals, which form the focus of the rest of the present work.

Weyl semimetals are materials that host gapless modes only at very specific momenta in the Brillouin zone. They have a myriad of properties that make them worthy subjects of study, not only from a theoretical perspective but also in potential experimental and engineering applications. Practically, Weyl semimetals have exotic transport properties such as a resistance which is highly sensitive to the application of a magnetic field, opening up countless possibilities for electronic applications.

Experimentally, Weyl semimetals may comprise the first platform in which the chiral fermions described by Herman Weyl in 1929 can be studied in the wild, in the form of bulk quasiparticle excitations—despite their mathematical simplicity, Weyl fermions do not appear to exist as fundamental particles in nature.

This aspect of Weyl semimetals is also of theoretical interest, since their fermionic modes may be altered in different ways beyond the simple description originally given by Weyl. Additionally, the topology of Weyl semimetals is intrinsically rich and generalises many aspects of insulator topology. It is this latter topological point of view which is the main focus of this chapter; the interested reader is referred to Refs. [\[Armitage\]](#) and [\[Hosur\]](#) for more complete physically-minded overviews.

This chapter does not contain any new results; instead, its purpose is to provide the necessary context for the results contained in Chapter 4. We begin by introducing the most important physical aspects of Weyl semimetals in Section 3.1, with a focus on the features that are of topological relevance. Section 3.2 then dives deeper into the underlying topology, introducing many of the relevant mathematical concepts at a fairly elementary level.

3.1 Physical aspects

The concept of Weyl semimetals arises naturally when studying how different energy bands relate to each other in three-dimensional solids. Whereas one and two-dimensional materials are generally gapped unless additional symmetries force the

bands to touch, the situation is different in three dimensions. In this context, so-called *accidental band crossings* are expected based on geometric arguments [Herring, 1937].

Accidental crossings can be understood by studying the interplay between any two of the energy bands. In most physically relevant scenarios these will be the valence and conduction band, since these determine the conductive properties of a material. Recall that the generic Hermitian two-band Hamiltonian can be written as

$$\mathcal{H}(\mathbf{k}) = h_0(\mathbf{k})\mathbb{I} + \mathbf{h}(\mathbf{k}) \cdot \boldsymbol{\sigma},$$

where \mathbf{k} lives in the three-dimensional Brillouin torus \mathbb{T}^3 in this case. The eigenvalues of this Hamiltonian are

$$E(\mathbf{k}) = h_0(\mathbf{k}) \pm |\mathbf{h}(\mathbf{k})| = h_0(\mathbf{k}) \pm \sqrt{h_1^2(\mathbf{k}) + h_2^2(\mathbf{k}) + h_3^2(\mathbf{k})},$$

so that the gap between the two bands closes exactly when $\mathbf{h}(\mathbf{k}) = 0$. That is, band crossings occur at the simultaneous zeroes of three functions h_i for $i \in \{1, 2, 3\}$, all depending on three momentum degrees of freedom. Such a system of three equations with three parameters generically has point-like solutions: the zeroes of each individual h_i normally form a surface in \mathbb{T}^3 , two such surfaces intersect in a set of curves, and the third surface intersects these curves in a set of points. This means that two bands in a three-dimensional system generically have point-like intersections where the gap closes, given that the bands are close enough together (i.e. the functions h_i each have zeroes to begin with). These band crossings are called accidental because they are not enforced by any symmetry of the system, but as we will review shortly, they are actually topologically robust and cannot be gapped out by small perturbations.

3.1.1 Weyl points

Near a band intersection at $\mathbf{k} = \mathbf{k}_w$, the Hamiltonian can be linearized: writing $\delta\mathbf{k} := \mathbf{k} - \mathbf{k}_w$, it can be expanded as

$$\mathcal{H}(\delta\mathbf{k}) = h_0(\mathbf{k}_w)\mathbb{I} + \mathbf{v}_0 \cdot \delta\mathbf{k}\mathbb{I} + \sum_{i=1}^3 \mathbf{v}_i \cdot \delta\mathbf{k} \sigma^i + \mathcal{O}(\delta\mathbf{k}^2), \quad (3.1)$$

where $(\mathbf{v}_\mu)_i := \partial_{k^i} h_\mu|_{\mathbf{k}=\mathbf{k}_w}$ records the rate of change of the different components of the Hamiltonian. The spectrum associated with this linear equation looks like two cones which touch at $\mathbf{k} = \mathbf{k}_w$, often collectively called the *Weyl cone*; see Figure [figure]. The different components of Equation (3.1) can all be given an interpretation in terms of this Weyl cone: for example, $h_0(\mathbf{k}_w)$ is the energy at which the bands touch, and it determines how far this crossing is from the Fermi energy $\varepsilon_F = 0$. If h_0 is sufficiently far from the Fermi level, the Fermi surface expands to connect with those around other band crossings and gains an extensive two-dimensional structure. Normal metallic dispersive behaviour dominates in this case. However, if h_0 is close enough to zero, then the Fermi surface around \mathbf{k}_w becomes approximately point-like, and there is a low-energy bulk conductive mode

at \mathbf{k}_w . In this case the point \mathbf{k}_w is called a *Weyl point* or *Weyl node*. When all of the crossings between the valence and conduction band have this property, the material is referred to as a *Weyl semimetal*.¹

This nomenclature is derived from the traceless \mathbf{v}_i term in Equation (3.1): it bears resemblance to the simple chiral fermions described by Herman Weyl in 1929 [Weyl, 1929],

$$H_{\pm} = \mp c \mathbf{p} \cdot \boldsymbol{\sigma},$$

where the speed of light c is replaced by the smaller effective velocities \mathbf{v}_i in different directions. In a Weyl semimetal, the aforementioned low-energy modes have similar dispersive properties to Weyl fermions. This is one of the reasons Weyl semimetals are a desirable object of study, especially since—despite their mathematical simplicity—Weyl fermions have not been observed as fundamental particles in nature.

One particularly interesting feature of Weyl fermions is that they have a non-zero chirality associated with them, which leads to certain non-conserved charges upon quantisation—this is known as the chiral anomaly. It turns out that a similar truth holds for the band crossings described by Equation (3.1). They feature an intrinsic chirality χ , which can be calculated in generic cases by collecting the velocities \mathbf{v}_i into a 3×3 matrix $V_i^j := (\mathbf{v}_i)_j$ and computing the sign of its determinant:

$$\chi = \text{sign} |V_i^j|, \quad (3.2)$$

giving a chirality of $\chi = \pm 1$. In special cases where the band crossing is non-linear, the chirality may take on other integer values; this is captured more generally using a Berry curvature integral on a two-dimensional sphere surrounding the Weyl point. In this light, Weyl points can be viewed as sources or sinks of the Berry field, with a quantized integer charge. This charge is topological in nature, which is exactly why Weyl points are robust to perturbations. The implications of this topological perspective will be explored in greater detail in Section 3.2.

A final feature of Equation (3.1) that bears mentioning is the inclusion of the \mathbf{v}_0 term. This term can be interpreted in terms of a tilting of the associated Weyl cone. For small \mathbf{v}_0 , the Fermi surface of a Weyl point remains point-like, and the dispersive properties of the virtual Weyl fermion aren't greatly affected. However, for large enough \mathbf{v}_0 , the Weyl cone may begin to intersect the Fermi level, causing electron and hole pockets to form on either side of the Weyl point; see Figure 3.1. This tipping of the Weyl cone induces significantly altered dispersion, leading to different electronic properties. Such materials are categorised separately as so-called *type II* Weyl semimetals. This distinction is purely physical, however; the different types of Weyl semimetals cannot be distinguished topologically.

3.1.2 Global features

One important restriction on Weyl semimetals is that the total chirality of all Weyl points in the Brillouin zone must sum to zero—that is, for every source of the Berry

¹The term *Weyl metal* is also sometimes used for materials in which the Fermi surface is not point-like due to large h_0 , but still confined to closed surfaces around the band crossings [13]. The topology of such Weyl metals is equivalent to that of their semimetal counterparts, and we will pay them no further mind.

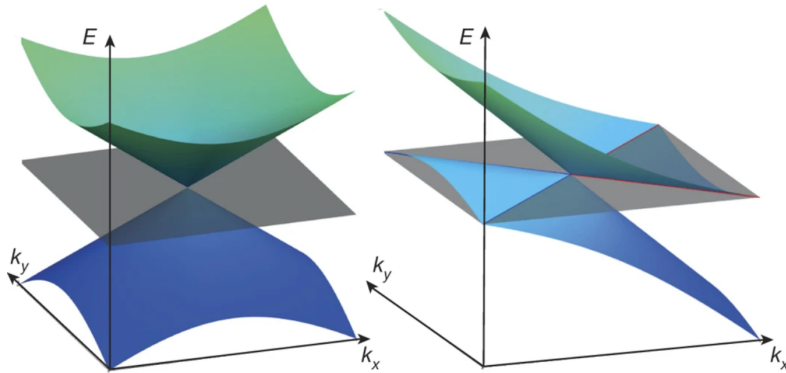


Figure 3.1: Figure from Ref. [14]. Left: Weyl cone in a normal (type I) Weyl semimetal. Right: “Overtilted” Weyl cone in a type II Weyl semimetal. Electron and hole pockets are outlined in red and blue, respectively.

field (Weyl point with $\chi > 0$) there must also be a sink ($\chi < 0$), and vice versa. This result is known as the Nielsen–Ninomiya theorem, after Holger Bech Nielsen and Masao Ninomiya who proved it in a more general context in 1981 [15, 16]. We will explore the topological nature of this theorem in more detail in Section 3.2. Physically, this charge cancellation is related to the aforementioned chiral anomaly: electric charge is locally non-conserved near a Weyl point under the application of electric and magnetic fields, and this effect must be cancelled by a Weyl point of the opposite chirality. More details on the chiral anomaly in Weyl semimetals are reviewed in Ref. [17].

The Nielsen–Ninomiya theorem is an indication that Weyl points must communicate with their opposite-chirality counterparts in some way to allow transport of charge. This connection manifests itself on the surface of a Weyl semimetal: there, gapless states called *Fermi arcs* appear in the form of curves connecting the projections of oppositely-charged Weyl points; see Figure 3.2. Fermi arcs serve as important experimental signatures of Weyl semimetals, and they have been observed in both electronic and artificial crystals since 2015 [18–22, 26]; see Figure 3.3.

3.1.3 Semimetals with symmetries

Thus far, we have discussed Weyl semimetals without assuming any additional symmetry constraints. However, real crystalline solids often naturally possess symmetries beyond simple translational symmetry. Two such symmetries which are especially relevant to the discussion of Weyl semimetals are time-reversal symmetry and inversion symmetry.

Inversion symmetry is a natural property of many real-space lattices: it implies that there is an inversion centre \mathbf{x}_0 in the unit cell around which the lattice is symmetric as $\mathbf{x} \leftrightarrow \mathbf{x}_0 - \mathbf{x}$. In momentum space, this symmetry acts on the Hamiltonian as

$$\mathcal{H}(\mathbf{k}) = U\mathcal{H}(-\mathbf{k})U^\dagger, \quad (3.3)$$

where U is some unitary transformation. In particular, this implies that a Weyl point

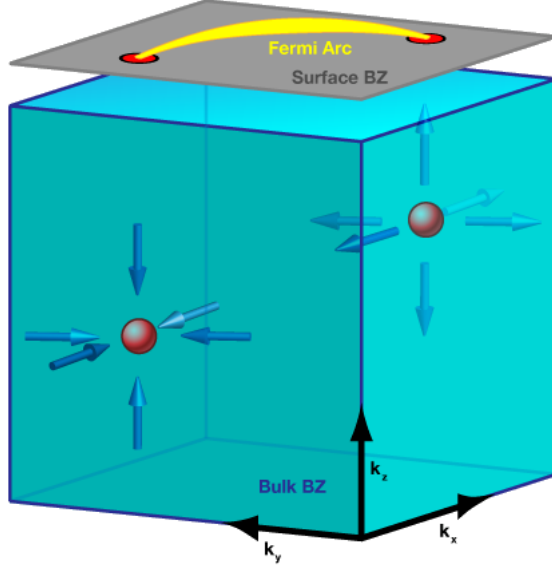


Figure 3.2: Figure by Alan Stonebraker. The 3D bulk Brillouin zone is shown of a Weyl semimetal with two Weyl points of negative and positive chirality, depicted as a sink and a source of the Berry field respectively. A 2D surface Brillouin zone is also depicted in grey at the top, featuring the projection of the two Weyl nodes connected by a Fermi arc of gapless states.

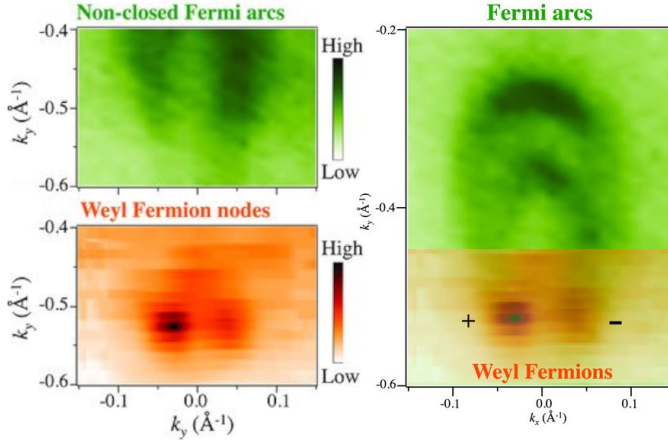


Figure 3.3: Figures from Ref. [21]. Experimental bulk (orange) and surface (green) Fermi surfaces, obtained through angle-resolved photoemission spectroscopy (ARPES). Bottom left: Two Weyl points appearing close together in the bulk. Top left: Fermi arcs are shown to terminate on the surface Brillouin zone above these Weyl points. Right: Bulk measurements are overlaid on the surface measurements at matching k_x and k_y values, showing good agreement between the position of the Weyl nodes and the tail ends of the Fermi arcs. In this case the two distinct Fermi arcs appear because there are two separate sets of Weyl nodes with the same k_x and k_y coordinates.

at $\mathbf{k} = \mathbf{k}_w$ has a partner at $\mathbf{k} = -\mathbf{k}_w$ with the opposite chirality. Take for example the case of $U = \mathbb{I}$ and a Weyl point with the simple linearized Hamiltonian

$$\mathcal{H}(\delta\mathbf{k}) = \sum_{i,j} V_i^j \delta k_j \sigma^i.$$

This point has chirality $\chi = \text{sign}|V_i^j|$, and Equation (3.3) implies that

$$\mathcal{H}(-\delta\mathbf{k}) = \sum_{i,j} (V')_i^j (-\delta k_j) \sigma^i = \mathcal{H}(\delta\mathbf{k}),$$

meaning there is a Weyl point at $\mathbf{k} = -\mathbf{k}_w$ with chirality $\chi' = \text{sign}|(V')_i^j| = \text{sign}|-V_i^j| = -\chi$. This reversal of chirality means Nielsen–Ninomiya is automatically satisfied under inversion symmetry. As a result, the minimum number of Weyl points in such a system is two; a Weyl point may be connected to its own symmetric partner via surface Fermi arcs.

Time-reversal symmetry has a similar action in momentum space, since momentum has a time component. It differs in the sense that time-reversal is an anti-unitary symmetry, meaning it also induces complex conjugation on the Hamiltonian:

$$\mathcal{H}(\mathbf{k}) = U \mathcal{H}^*(-\mathbf{k}) U^\dagger.$$

This complex conjugation changes the sign of the σ^2 term in the Hamiltonian; for Weyl points, this changes the sign of \mathbf{v}_2 , inducing a sign change in the determinant of V_i^j . This cancels the sign change discussed above, meaning a Weyl point at $\mathbf{k} = \mathbf{k}_w$ always comes with a symmetric partner of *equal* chirality at $\mathbf{k} = -\mathbf{k}_w$. Such a pair of equal-chirality points is sometimes referred to as a *Kramers pair*. The presence of Kramers pairs means the minimum number of Weyl points in a time-reversal invariant Weyl semimetal is four: following Nielsen–Ninomiya, a pair of $\chi = +1$ points must always be accompanied by a pair of $\chi = -1$ points and vice versa.

The fact that the chirality of Weyl points is reflected in different ways under inversion and time-reversal symmetry immediately implies that a Weyl semimetal cannot satisfy both symmetries at once: if a Weyl point has a non-zero chirality χ , then inversion implies its partner has chirality $-\chi$, while time-reversal implies it should have chirality χ . Physically, this is because the combination of inversion and time-reversal induces a spin degeneracy in the band structure, making modes of opposite chiralities coincide. This is in close analogy to the way in which a Dirac fermion combines two Weyl fermions of opposite chirality into a single description; this is precisely why band touching points of this nature are called *Dirac cones*, and systems featuring them are referred to as *Dirac semimetals*. Because of the lack of non-zero chiralities, such materials are topologically less rich than their Weyl counterparts, and we will not expand on them further.

All in all, a candidate Weyl semimetallic material must break either inversion or time-reversal symmetry. Of the two, breaking time-reversal symmetry is conceptually simpler in theory: the minimum amount of Weyl points is lower, and the symmetry is straightforwardly broken in the presence of a magnetic field. However, in practice the experimental detection of Fermi arcs and other spectral features relies on angle-resolved photoemission spectroscopy (ARPES), which is sensitive to magnetic fields. This is why to date, all experimentally confirmed electronic Weyl semimetals have preserved time-reversal symmetry and broken inversion symmetry instead [18–22].

3.2 Topological description

In all the systems studied in Chapter 2, the underlying approach to topological classification has been to study which band structures cannot be deformed into each other without closing the band gap anywhere in the Brillouin zone. Weyl semimetals already feature band crossings in the bulk to begin with, meaning this approach needs to be modified. The basic idea involves fixing a number of gapless points in place first, and then studying what gapped topologies are admitted on the rest of the Brillouin zone outside of these points. There are many intricacies to this idea, some of which we attempt to review pedagogically in this section.

Though most of the experimental candidates for Weyl semimetals feature either inversion or time-reversal symmetry, the conceptual topology framework is simplest in the absence of any symmetries beyond lattice translation. The majority of this section is written with this context in mind. Most of the concepts here are borrowed from two superb (if fairly technical) works by Vargese Mathai and Guo Chuan Thiang [23, 24].

Only in the final part of this section will we return to time reversal symmetric systems, and review how the inclusion of this symmetry alters the topological description. This provides important context to our treatment of other symmetries in Chapter 4.

The topological arguments in this section rely heavily on the concepts of cohomology and homology. Where possible, an attempt is made to explain the relevant ideas “just enough” in their proper physical context so that the main flow of the text may be followed without the relevant mathematical background. Readers seeking a somewhat more fundamental understanding are invited to refer to Appendix A as needed.

3.2.1 3D Chern insulators

To get a good intuition for the topological description of Weyl semimetals, it is useful to first consider a fully insulating material with similar properties. Suppose we have a three-dimensional material that is not subject to any additional symmetries. Such a material is called a 3D Chern insulator [25–27], in analogy to the 2D Chern insulator studied in Section 2.4.1. This system is not a semimetal, but it provides the relevant topological backdrop: Weyl semimetals can be obtained by letting the bands touch in a 3D Chern insulator. As we will discuss shortly, this allows them to act as transitional phases between different insulating topological states.

From the Atland-Zirnbauer classification in Table [reference], one might expect such a 3D type A system to be topologically trivial. However, as seen before in Equation [reference] (and perhaps also in 3D BHZ/Kane-Mele if I discuss this in ch. 2), the full topological classification of materials depends not only on the top-dimensional topology, but also on that borrowed from lower-dimensional subspaces. In the case of a 3D Chern insulator, this topology arises on two-dimensional slices of the Brillouin zone; an example of such a slice is highlighted in Figure 3.4.

There are three topologically distinct ways to slice up the three-torus, all perpen-

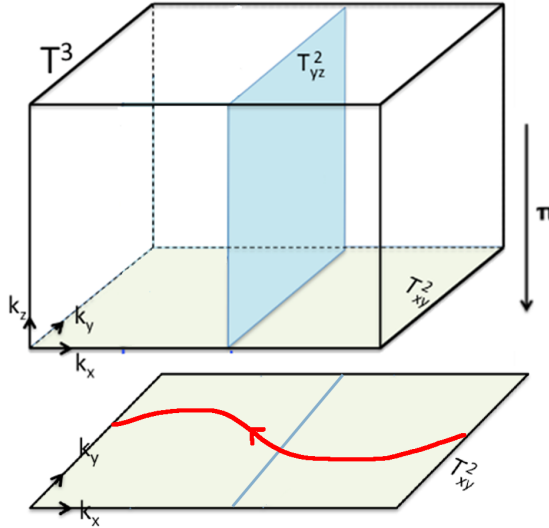


Figure 3.4: Figure adapted from Ref. [23]. The three-dimensional Brillouin torus \mathbb{T}^3 of a Chern insulator is shown, with a two-dimensional slice \mathbb{T}_{yz}^2 indicated in blue. A projection onto a surface Brillouin zone in the xy -direction is also shown, with an example Fermi loop of gapless states in red. In this example, the slice \mathbb{T}_{yz}^2 has a Chern number of $C_x = 1$. Hence, its projection onto the surface is a 1D loop (blue line) that features one chiral band crossing.

dicular to one of the three coordinate directions.² These slices have the topology of a two-torus \mathbb{T}^2 , and a Chern number can be obtained by integrating the Berry curvature \mathcal{F} of the system over them: for example, perpendicular to the x direction there is a Chern number³

$$C_x = \frac{1}{2\pi} \int_{\mathbb{T}_{yz}^2} \mathcal{F}.$$

This results in a classification by three distinct Chern numbers C_x , C_y and C_z , which are commonly arranged in a so-called *Chern vector*

$$\mathbf{C} = \begin{pmatrix} C_x \\ C_y \\ C_z \end{pmatrix} \in \mathbb{Z}^3.$$

Importantly, these three Chern numbers are all induced by a single two-form \mathcal{F} . In this sense, there is an exact correspondence between topologically distinct Berry curvatures \mathcal{F} and Chern vectors $\mathbf{C} \in \mathbb{Z}^3$. This is precisely what motivates the use of cohomology for classification: just like in the 2D Chern insulator, the two-form \mathcal{F}

²Other 2D slices exist, such as those going diagonally across, but these can all be considered linear combinations of the three “orthogonal” slices. To be precise, the different classes of 2D subspaces of \mathbb{T}^3 form the second homology group $H_2(\mathbb{T}^3) \cong \mathbb{Z}^3$, and this group is *generated* by the orthogonal slices.

³Note that it does not matter where along the Brillouin zone the yz -slice \mathbb{T}_{yz}^2 is taken: the Chern number is an integer, while the system is continuous. This means the x coordinate can be changed continuously without changing the resulting Chern number.

can be considered to represent a class in the second cohomology group,⁴

$$[\mathcal{F}] \in H^2(\mathbb{T}^3) \cong \mathbb{Z}^3. \quad (3.4)$$

As a result, this group precisely classifies the distinct topological phases of the system.⁵

Boundary states

Before moving on to a system with Weyl points, it will be instructive to study the gapless modes that arise on the surface of a 3D Chern insulator with non-zero Chern vector. Figure 3.4 illustrates the case where $\mathbf{C} = (1, 0, 0)^T$. In this case, \mathbb{T}_{yz}^2 is the only orthogonal slice with a non-zero Chern number, and as such the material lattice can be thought of as a stack of 2D Chern insulators spanning the y and z directions, stacked together in the x direction. \mathbb{T}_{yz}^2 can effectively be considered the Brillouin zone of such a 2D Chern insulator.

Recall from our discussion in Section 2.4.1 that a 2D Chern insulator with a Chern number of 1 has a single chiral edge mode, which manifests as a gapless state on the one-dimensional surface Brillouin zone. This logic can be translated to the three-dimensional case, where such slices are stacked in the x direction. Suppose there is a projection π along the z direction, onto a two-dimensional surface Brillouin zone $\tilde{\mathbb{T}}_{xy}^2$. Then the two-dimensional slices \mathbb{T}_{yz}^2 project down to a one-dimensional loop $\pi(\mathbb{T}_{yz}^2) \cong S^1$ containing a single point-like gapless state. As the \mathbb{T}_{yz}^2 slice is moved around in the x direction, this band crossing point moves continuously along the y direction, by continuity of the Hamiltonian. It follows that the full two-dimensional surface Brillouin zone must contain a loop of gapless states going across the x direction, as depicted in the figure. This loop is called a *Fermi loop*, in analogy with the Fermi arcs in a Weyl semimetal. Moreover, the chirality of the edge modes can be used to assign a consistent orientation to this loop.

Fermi loops admit a natural topological description in terms of homology. Being oriented loops, they precisely represent a class in the first homology group $H_1(\tilde{\mathbb{T}}^2)$ of the surface Brillouin zone. Furthermore, it is possible to define an oriented *Dirac loop* ℓ in the bulk Brillouin zone in such a way that its projection $\pi(\ell)$ onto the surface in any direction is exactly the Fermi loop. This loop ℓ is not a gapless feature,⁶ but it is rather interesting topologically: it represents a first homology class in the bulk Brillouin zone,

$$[\ell] \in H_1(\mathbb{T}^3) \cong \mathbb{Z}^3.$$

⁴As explained in Appendix A, \mathcal{F} more properly represents a class in the real-valued *de Rham cohomology* group $H_{dR}^2(\mathbb{T}^3) \cong \mathbb{R}^3$. The analogy is strong enough to be considered direct here, but de Rham cohomology is too plain to encode features such as \mathbb{Z}_2 invariants. This is why we make use of the richer integer-valued cohomology theory.

⁵More fundamentally, a complex vector bundle called the *valence bundle* can be associated to a gapped Hamiltonian, and the second cohomology group classifies the different complex vector bundles over a manifold.

⁶Dirac loops do still admit a physical interpretation: they represent points at which the Berry connection \mathcal{A} has a gauge singularity. Such singularities depend on the choice of gauge, meaning the loop can be moved around by gauge transformations; however, this does not change their topology. The same goes for the Dirac strings that will be discussed in a moment.

It is not a coincidence that this first homology group is isomorphic to the second cohomology group $H^2(\mathbb{T}^3)$ from Equation (3.4). This equivalence is a result of *Poincaré duality*, which is the statement that for any closed oriented d -dimensional manifold M , the isomorphism

$$H_n(M) \cong H^{d-n}(M)$$

holds for any integer n . In the present case, this duality can be stated intuitively in terms of Chern numbers, which count the number of signed intersections of the Dirac loop with the different two-dimensional slices of the Brillouin zone.⁷ This duality can be summarised schematically as follows:

$$H^2(\mathbb{T}^3) \ni [\mathcal{F}] \xrightleftharpoons{\text{integration}} \mathbf{C} \xrightleftharpoons{\text{intersections}} [\ell] \in H_1(\mathbb{T}^3). \quad (3.5)$$

This Poincaré duality ensures that the classifications in terms of first homology and second cohomology are completely equivalent in this case. Importantly, however, Poincaré duality depends on orientability, and it will not hold when we consider non-orientable Brillouin zones in the next chapter. As such, the question of which group provides the right classification of such a system will be key. For the moment, we turn our attention to the topology of Weyl points in the simpler orientable setting.

3.2.2 Topology with Weyl points

Consider a Weyl semimetal with a set of k Weyl points

$$W \equiv \{w_1, w_2, \dots, w_k\} \subset \mathbb{T}^3.$$

Then the charge of a Weyl point w_i is given by the Chern number

$$C_w = \frac{1}{2\pi} \int_{S_w^2} \mathcal{F},$$

where S_w^2 is a sufficiently small 2-sphere centred at w —in particular, it must be small enough to contain no other Weyl points in its interior. Naively, this might lead us to expect that a semimetal phase is classified by the second cohomology group of the collection of all these spheres:

$$H^2 \left(\bigcup_{i=1}^k S_{w_i}^2 \right) \cong \bigoplus_{i=1}^k H^2(S_{w_i}^2) \cong \mathbb{Z}^k. \quad (3.6)$$

However, this classification runs into two problems: it ignores the global cancellation of charge, and it also ignores the additional topology on two-dimensional slices discussed in the previous subsection. Both of these issues are due to the fact that this group only captures the *local* topology near each Weyl point, and they can be

⁷In general, it is possible that a single Dirac loop “folds back on itself” and intersects such a slice more than once. However, any additional intersections introduced in this way always come in oppositely-oriented pairs, leaving the topology unchanged.

addressed by studying how the different Chern numbers on the Brillouin zone must relate to each other *globally*.

The Nielsen–Ninomiya charge cancellation theorem is one such global relation. It is the statement that all the Chern numbers on these 2-spheres must add to zero:

$$\sum_{i=1}^k C_{w_i} = 0. \quad (3.7)$$

This cancellation can be demonstrated using Stokes’ theorem. The argument goes as follows: imagine that the interior of each sphere $S_{w_i}^2$ (i.e. a small open 3-ball centred at w_i) is removed from \mathbb{T}^3 . The resulting 3-manifold X looks like a 3-torus with k small ball-shaped holes, and its boundary is given by the collection of spheres:

$$\partial X = - \bigcup_{i=1}^k S_{w_i}^2,$$

where the minus sign induces the correct orientation. Then Stokes’ theorem gives

$$0 = \frac{1}{2\pi} \int_{\partial X} d\mathcal{F} = - \sum_{i=1}^k \frac{1}{2\pi} \int_{S_{w_i}^2} \mathcal{F} = - \sum_{i=1}^k C_{w_i},$$

which is precisely the Nielsen–Ninomiya theorem.

A similar argument can also be applied to study what happens to Chern numbers on two-dimensional slices of the Brillouin zone in this context. This argument is illustrated in Figure 3.5. Here, two slices \mathbb{T}_L^2 and \mathbb{T}_R^2 are placed on either side of

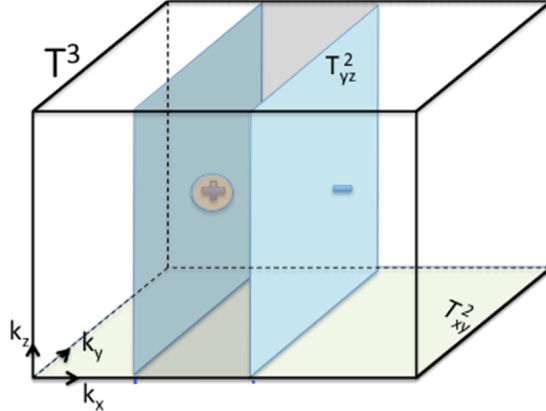


Figure 3.5: Brillouin torus \mathbb{T}^3 of a Weyl semimetal with two oppositely charged Weyl points labelled + and -. Three two-dimensional subspaces are indicated in blue: a yz -like 2-torus on either side of the + point, and a small 2-sphere surrounding it. Given the proper orientation, the blue spaces form the boundary of a three-dimensional manifold Y , shaded in grey here. Figure from Ref. [23]. [not yet licensed; may need better labelling]

a Weyl point w with charge $C_w = q$, along with a small sphere S_w^2 surrounding it.

These spaces then bound a three-dimensional manifold Y as indicated in the figure, given the following orientations:

$$\partial Y = \mathbb{T}_R^2 - \mathbb{T}_L^2 - S_w^2.$$

The same Stokes' theorem argument can then be used to relate the Chern numbers C_L and C_R on the respective slices, yielding

$$C_R = C_L + C_w = C_L + q.$$

That is, the Chern number of a two-dimensional slice increases by q every time it passes over a Weyl point with charge q . As a sanity check, it should be noted that this process respects the periodicity of the Brillouin torus: when the slice is passed over the entire torus, charge cancellation ensures that the added Chern number is zero in total.

All in all, the presence of Weyl points allows for a finer collection of Chern numbers to appear in the Brillouin zone, beyond the \mathbb{Z}^3 Chern vector of the insulating case. This behaviour can be captured using cohomology. The key idea is that the Berry curvature has a singularity at points where the gap closes.⁸ As such, it can only be integrated over subspaces where the gap never closes, so that the set of Weyl points W needs to be excluded. This means \mathcal{F} now lives in the second cohomology group of the Brillouin zone minus W :

$$[\mathcal{F}] \in H^2(\mathbb{T}^3 \setminus W) \cong \mathbb{Z}^3 \oplus \mathbb{Z}^{k-1}, \quad (3.8)$$

where k again is the number of Weyl points. Put differently, classification of semimetallic phases given a set of Weyl points W essentially amounts to classifying the gapped phases on the punctured torus $\mathbb{T}^3 \setminus W$.

Notably, this classification addresses both issues present in the \mathbb{Z}^k classification on 2-spheres in Equation (3.6). Firstly, it incorporates 3D Chern insulator topology in the first term, in the form of the \mathbb{Z}^3 from Equation (3.4). Perhaps more subtly, charge cancellation is also incorporated in the form of the reduction by one \mathbb{Z} factor in the second term. This can be understood intuitively: for example, if $k = 1$ then the Nielsen–Ninomiya theorem implies that the single Weyl point must have a charge of 0, and so it is not topologically protected. A similar intuition holds for larger k , in that the k “degrees of freedom” which are afforded to the system by the Weyl point charges are reduced by one under the charge cancellation condition. This relation will become more explicit once the Mayer–Vietoris sequence is introduced in Section 3.2.3.

Fermi arcs

The varying Chern numbers over Weyl points help explain how Fermi arcs arise on the surface. As discussed in the case of a 3D Chern insulator, Fermi loops on the surface arise whenever there is a non-zero Chern number in some direction. Similarly, Fermi arcs begin and terminate whenever the presence of a Weyl point causes a change in the Chern number; this is illustrated in Figure 3.6.

⁸Note that this singularity is required in order for the Chern number to change suddenly when a slice (i.e. the integration domain of \mathcal{F}) is moved over a Weyl point continuously.

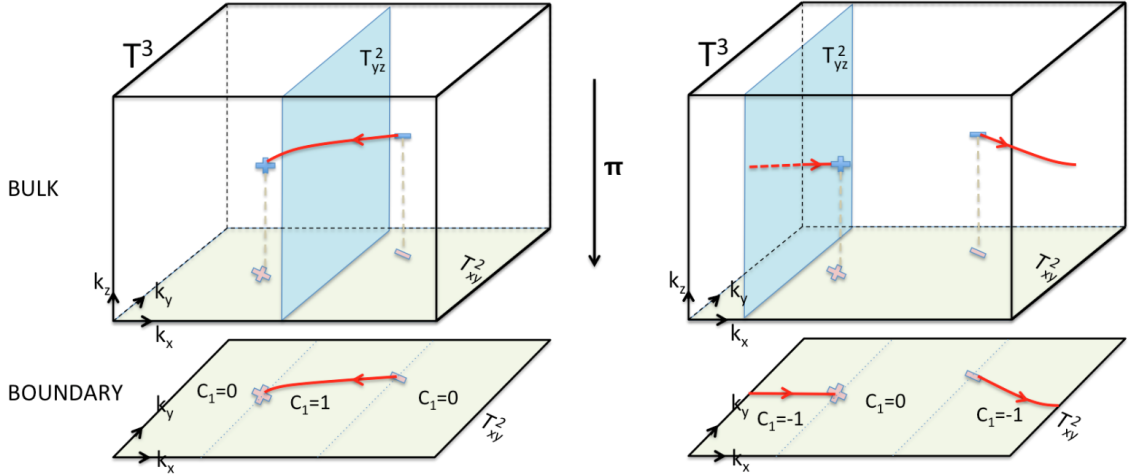


Figure 3.6: Two semimetal Brillouin zones are shown with the same configuration of Weyl points, but featuring topologically distinct Fermi arcs (shown in red on the boundary). The distinction is due to different bulk Chern numbers: Fermi arcs appear in regions where the bulk Chern number is non-zero. These Fermi arcs can be considered to be the projection of a Dirac string (shown in red in the bulk). Figure from Ref. [23].

This feature of Weyl semimetals implies they can mediate phase transitions between 3D Chern insulators with different Chern vectors. For example, suppose a pair of Weyl points is created at some point in the Brillouin zone of a trivial insulator ($\mathbf{C} = 0$). These points can then be moved apart in the z direction until they meet again and annihilate at the other end of the torus. In the process, a Fermi arc extends between the projections of the Weyl points on the xz and yz -planes, which eventually closes into a Fermi loop. In its final state, the system features a non-zero Chern vector of $\mathbf{C} = (0, 0, 1)^T$.

This process was first observed experimentally in a seminal work by Gui-Geng Liu et al. in 2022 [26]. The authors construct a photonic crystal, which is a type of artificial crystal where the different energy levels are represented by frequencies of light. Under application of a magnetic field, this crystal undergoes a transition between trivial and topological insulating phases, mediated by the creation and annihilation of two Weyl points; see Figure 3.7. This was also the first experimental realisation of a 3D Chern insulator, and of a system featuring a single Fermi arc.

Just as Fermi loops can be considered projections of a bulk Dirac loop, so too can Fermi arcs be considered a projection of a bulk *Dirac string*.⁹ Like Dirac loops, these strings can be given an interpretation in terms of homology. The setup is somewhat more subtle in this case: since the Dirac strings have a boundary, they are not loops and as such do not represent homology classes in $H_1(\mathbb{T}^3)$. Instead, they represent classes in the *relative homology group*

$$H_1(\mathbb{T}^3, W) \cong \mathbb{Z}^3 \oplus \mathbb{Z}^{k-1} \quad (3.9)$$

⁹A more or less equivalent concept is referred to as *Euler chain* in Ref. [23], placing the emphasis on topology over physics: “chain” here refers the oriented subspaces that homology is founded on.

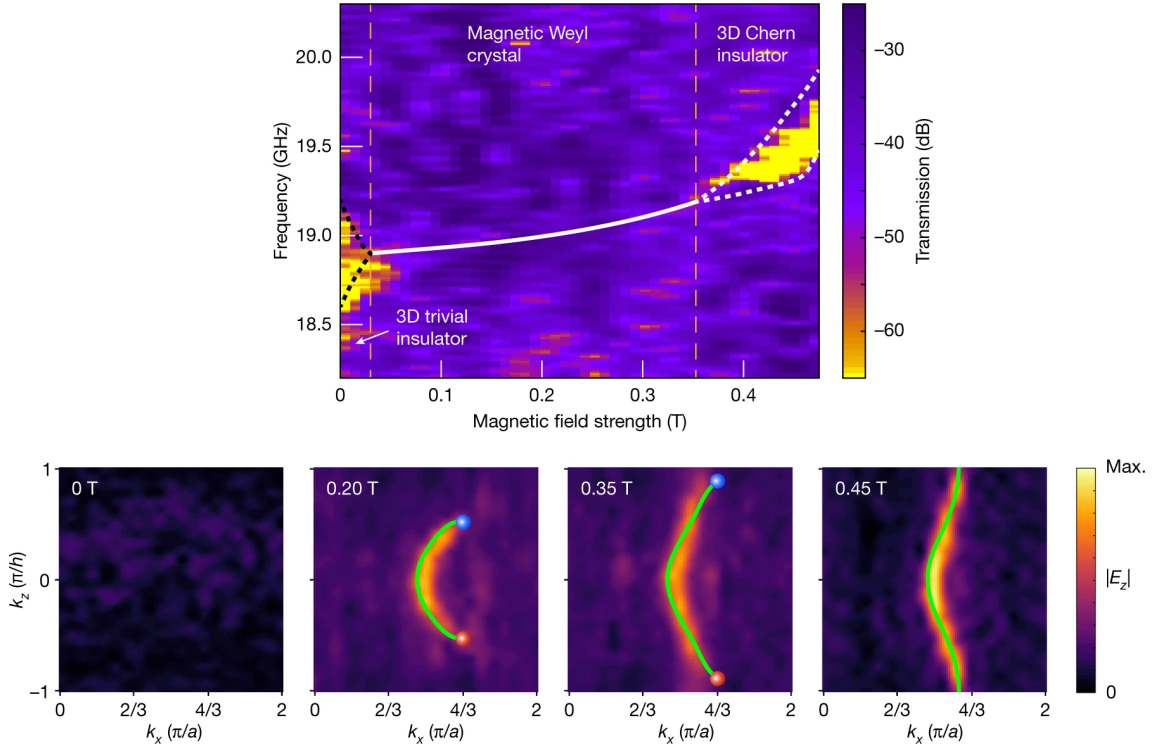


Figure 3.7: Figure from Ref. [26], reproduced with permission from Springer Nature. Top: measured frequency response (i.e. “band structure”) at increasing magnetic field strength. Yellow regions represent a band gap in the spectrum, indicating insulating phases. The white line represents the calculated frequency of the two Weyl nodes in the system. Bottom: measured response on a surface Brillouin zone, at the frequencies indicated on the white line above. Simulated Fermi arcs and loops are shown in green. A Fermi loop can clearly be seen to form, confirming a phase change to a topological insulator.

with respect to the set of Weyl points $W \subset \mathbb{T}^3$. Intuitively, taking the relative homology means that any boundaries lying in the subset W are ignored; for a more precise definition the reader is referred to Ref. [28, §2.1].

This homology picture provides a classification scheme that is exactly dual to the cohomology classification in Equation (3.8); that is, there is an isomorphism

$$H^2(\mathbb{T}^3 \setminus W) \cong H_1(\mathbb{T}^3, W). \quad (3.10)$$

This is not a direct Poincaré duality, but it is nevertheless mathematically rigorous and protected by orientability in the same way.¹⁰ The interpretation in terms of Chern numbers given in Equation (3.5) also still holds here, with the Chern vector and Dirac loops replaced with more general Chern numbers and Dirac strings, respectively.

¹⁰To be precise, Poincaré duality does not hold directly because $\mathbb{T}^3 \setminus W$ is not a closed manifold. Instead, for non-compact manifolds M there is a generalized duality $H^n(M) \cong H_{d-n}^{\text{BM}}(M)$ where the group on the right is the *Borel-Moore homology*, and this is in turn equivalent to the relative homology in this case. Alternatively, Equation (3.10) can be interpreted as a result of the so-called *Lefschetz duality* $H^n(M) \cong H_{d-n}(M, \partial M)$ for manifolds with a boundary.

3.2.3 The semimetal Mayer–Vietoris sequence

In the previous section, a heuristic Stokes’ theorem argument was presented for charge cancellation on Weyl points. This argument can be generalized by moving to a more abstract cohomology setting, where we are not dependent on the integration of forms; this is important because integration will not be well defined once we move to a non-orientable setting. As an added bonus, the abstract description proves to be richer and provide more detailed information on the possible topological phases for a Weyl semimetal.

The idea is that the relation between the global semimetal topology in Equation (3.8) and the local charge data in Equation (3.6) can be understood by considering how cohomology classes are mapped between them. That is, one needs to find and study a homomorphism

$$\beta : H^2(\mathbb{T}^3 \setminus W) \rightarrow H^2\left(\bigcup_{i=1}^k S_{w_i}^2\right).$$

Such a map arises naturally in the context of the *Mayer–Vietoris sequence* for cohomology.

Mayer–Vietoris sequences are used to study how the homology or cohomology of a topological space relates to that of its subspaces. To be precise, let X be a topological space and let $A, B \subset X$ be two subspaces that cover it (i.e. $A \cup B = X$). Then, there is an *exact sequence* of homomorphisms between cohomology groups,

$$\cdots \rightarrow H^n(X) \rightarrow H^n(A) \oplus H^n(B) \rightarrow H^n(A \cup B) \rightarrow H^{n+1}(X) \rightarrow \cdots,$$

which continues indefinitely in both directions. Exactness means that the image of each map in the sequence is exactly equal to the kernel of the next. In other words, the elements in each term in the sequence which are mapped to zero in the next term are precisely those which “descend” from the previous term. In particular, the composition of two subsequent maps always yields zero.

In the context of a Weyl semimetal, there is a natural way to divide the Brillouin torus \mathbb{T}^3 into two subspaces; this is illustrated in Figure 3.8. The first subspace in the covering is the punctured torus $\mathbb{T}^3 \setminus W$; we have already encountered this space in classifying topological semimetal phases. The other is the collection $\bigcup_{i=1}^k D_{w_i}^3$ of small open 3-balls centred on the Weyl points w_i . The intersection of these two spaces is the same collection of open balls, but each with a single puncture. For our purposes, this intersection has the same topology as the collection of 2-spheres $\bigcup_{i=1}^k S_{w_i}^2$ that we encountered in the context of local Weyl point charges.¹¹ A Mayer–Vietoris sequence can now be written down for these subspaces. The section of this sequence which is

¹¹To be precise, the punctured 3-balls can be *deformation retracted* into the 2-spheres, making them *homotopy equivalent*. Homotopy equivalent spaces have the same homology and cohomology groups.

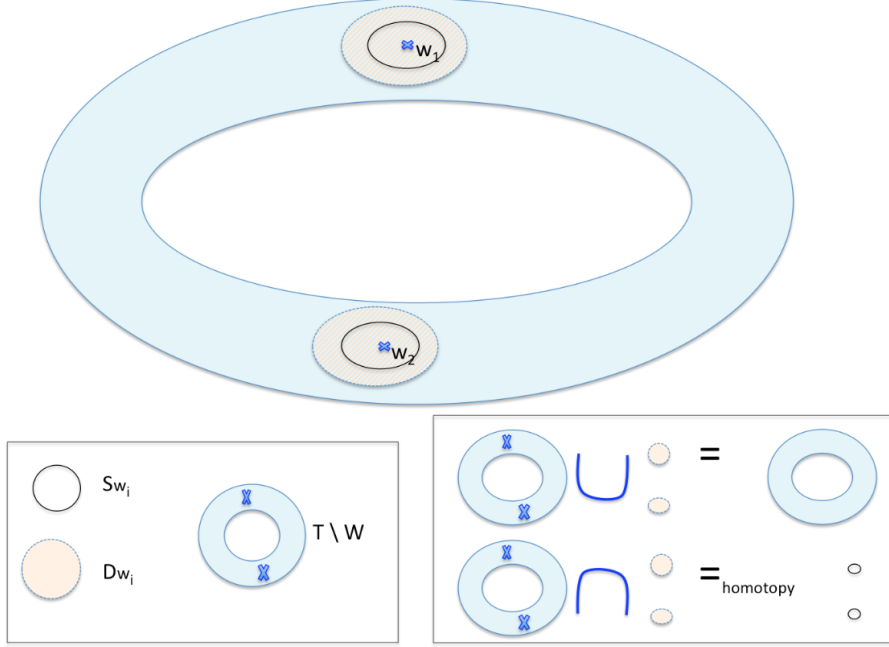


Figure 3.8: Schematic two-dimensional representation of the Brillouin torus and the subspaces used to cover it. Figure from Ref. [29].

relevant to classification is referred to as the *semimetal Mayer–Vietoris sequence*:¹²

$$0 \rightarrow \underbrace{H^2(\mathbb{T}^3)}_{\text{3D Chern insulator}} \rightarrow \underbrace{H^2(\mathbb{T}^3 \setminus W)}_{\text{Semimetal}} \xrightarrow{\beta} \underbrace{H^2\left(\bigcup_{i=1}^k S_{w_i}^2\right)}_{\text{Local charges}} \xrightarrow{\Sigma} H^3(\mathbb{T}^3) \rightarrow 0. \quad (3.11)$$

The first three groups in this sequence are already familiar from Equations (3.4), (3.8), and (3.6) respectively. [The comma before respectively is not necessary in British English, which I'm writing in (similarly for things like i.e. and e.g.)] The last group $H^3(\mathbb{T}^3) \cong \mathbb{Z}$ is represented by volume forms¹³ on the torus; one notable example of such a form is the trivial 3-form

$$d\mathcal{F} = 0 \in H^3(\mathbb{T}^3)$$

which appeared in the Stokes' theorem arguments previously. Indeed, the map labelled Σ above can be loosely interpreted as the exterior derivative d . However, a more physically useful interpretation is that Σ gives the total charge in the system: it sends a set of Chern numbers on the Weyl points to their sum in \mathbb{Z} .

Explicitly, the semimetal Mayer–Vietoris sequence is¹⁴

$$0 \rightarrow \mathbb{Z}^3 \rightarrow \mathbb{Z}^3 \oplus \mathbb{Z}^{k-1} \xrightarrow{\beta} \mathbb{Z}^k \xrightarrow{\Sigma} \mathbb{Z} \rightarrow 0. \quad (3.12)$$

¹²Note that the open balls $D_{w_i}^3$ do not appear in this sequence at all. This is because they can be contracted to a point, and hence are topologically trivial in a sense.

¹³I.e. 3-forms, which are locally proportional to $dk_x \wedge dk_y \wedge dk_z$.

¹⁴In principle the direct sum in the semimetal group has little mathematical significance; we write $\mathbb{Z}^3 \oplus \mathbb{Z}^{k-1}$ instead of \mathbb{Z}^{k+2} to aid the physical interpretation.

The exactness of this sequence can be used to extract useful information, especially around the group of local charges \mathbb{Z}^k . Here, exactness means that $\text{im}(\beta) = \ker(\Sigma)$. This implies that the local charges on the Weyl points sum to zero if and only if they descend from a semimetal. In other words, it implies not only the Nielsen–Ninomiya charge cancellation theorem, but also its converse: any set of Weyl points with charges adding to zero is admissible as a topological Weyl semimetal phase.

In fact, more can be inferred by looking at the maps around the semimetal group $\mathbb{Z}^3 \oplus \mathbb{Z}^{k-1}$. Here, exactness tells us that $\ker(\beta) \cong \mathbb{Z}^3$. This makes physical sense: if all local charges are zero, the Weyl points are not topologically protected and the system is really in a 3D Chern insulator phase. However, since β is a homomorphism, we also find $\beta^{-1}(c) \cong \mathbb{Z}^3$ for a generic charge configuration $c \neq 0 \in \mathbb{Z}^k$; that is, every configuration with total charge zero admits a \mathbb{Z}^3 worth of topologically different semimetal phases. This makes precise a principle that is also hinted at in Figure 3.6: Weyl semimetals with identical charge configurations may nevertheless be topologically distinct, and their topologies differ by a bulk Chern vector in \mathbb{Z}^3 .¹⁵

The dual homology sequence

In previous subsections, we have already seen that the cohomology invariants on Chern insulators and Weyl semimetals can be understood equally well in terms of homology groups. As it turns out, this duality can be extended to the semimetal Mayer–Vietoris sequence (3.11). The dual of the first two groups was already explored in Equations (3.5) and (3.10). The latter two groups act on closed manifolds, and so their dual can be obtained from Poincaré duality directly:

$$H^2\left(\bigcup_{i=1}^k S_{w_i}^2\right) \cong H_0\left(\bigcup_{i=1}^k S_{w_i}^2\right), \quad H^3(\mathbb{T}^3) \cong H_0(\mathbb{T}^3).$$

In both cases, we have a top-dimensional cohomology group (containing volume forms) being dualised to a zeroth homology group, which counts the number of connected components. In particular, since the connected components are the important aspect, the 2-spheres S_w may be substituted for the Weyl points w to simplify:

$$H_0\left(\bigcup_{i=1}^k S_{w_i}^2\right) \cong H_0(W).$$

The complete homology dual of (3.11) is then

$$0 \rightarrow \underbrace{H_1(\mathbb{T}^3)}_{\text{Dirac loops}} \rightarrow \underbrace{H_1(\mathbb{T}^3, W)}_{\text{Dirac strings}} \xrightarrow{\partial} \underbrace{H_0(W)}_{\text{Local charges}} \xrightarrow{\Sigma} H_0(\mathbb{T}^3) \rightarrow 0. \quad (3.13)$$

This exact sequence has arisen through taking Poincaré duals of groups in the Mayer–Vietoris sequence, but somewhat miraculously, it continues to be valid even in the absence of Poincaré duality (e.g. on a non-orientable manifold). In fact, it can be

¹⁵Properly speaking, the set of topological phases for a given charge configuration is an affine space for $H^2(\mathbb{T}^3)$, since there is no canonical zero Chern vector on a Weyl semimetal. This is worked out in greater mathematical detail in Section 3 of Ref. [23].

considered a more fundamental sequence in some ways: it describes the homology of the torus with respect to a single subspace W , whereas the Mayer–Vietoris sequence relies on multiple subspaces that cover the torus.¹⁶

The map indicated by ∂ is the boundary map that is used to define homology groups in the first place.¹⁷ In this case, it sends classes of oriented Dirac strings in the bulk to the Weyl points that bound them, with a sign given by which end of the string the points are on. For example, for a Weyl semimetal with two Weyl points $W = \{w_1, w_2\}$ connected by a Dirac string s , we have $[s] \in H_1(\mathbb{T}^3, W)$ and

$$\partial([s]) = (1, -1) \in H_0(W) \cong \mathbb{Z}^2.$$

This gives rise to a very natural interpretation of charge cancellation: it automatically follows from the fact that Weyl points on opposite ends of a Dirac string are assigned opposite signs. These opposite charges are then summed to zero by the total charge map Σ , i.e. $\Sigma \circ \partial = 0$. This can also be inferred from the exactness of (3.13), which additionally tells us that there exists a configuration of Dirac strings compatible with any set of Weyl points with total charge zero.

As emphasised before, this homology sequence encodes exactly the same information as the cohomology Mayer–Vietoris sequence in the simple case where Poincaré duality is preserved. However, once symmetries are imposed on the system, this duality may be altered, in which case the two basic sequences become essentially different. It then becomes necessary to study how the cohomology and/or homology groups must be altered to encode relevant information about the topological phases of the system. We will review one example of this in the next section.

3.2.4 Time-reversal symmetric Weyl semimetals

The preceding topological review of Weyl semimetals has thus far been in the context of the basic symmetry class A—that is, we have not imposed any additional symmetries on the system. However, such additional symmetries are not necessarily forbidden in a Weyl semimetal: the type A classification merely tells us that the semimetal topology is very robust, not relying on any symmetry protection.¹⁸ As discussed in Section 3.1, all of the experimentally observed electronic Weyl semimetals actually preserve time-reversal symmetry, which is a natural condition in the absence of a magnetic field. An excellent topological description of such systems was published by Guo Chuan Thiang, Koji Sato and Kiyonori Gomi in 2017, and we will spend the rest of this section reviewing its main aspects [29].

Time-reversal symmetric systems belong to class AII of the tenfold way classification in Table [cite table], meaning the underlying insulating topology (i.e. the topology with zero Weyl points) is that of the strong and weak insulators described in Section 2.4.3. This means the four \mathbb{Z}_2 invariants (three weak and one strong) in such

¹⁶Indeed, this is the first exact sequence introduced in the standard algebraic topology textbooks, e.g. in Theorem 2.13 of Ref. [28].

¹⁷To be precise, homology is defined using boundaries of chains; one can think of the present map as acting on *representatives* of homology classes.

¹⁸By contrast, for example, the SSH model introduced in Section 2.2 has chiral symmetry-protected topological phases.

systems also play a role in the semimetal topology. Just as class A Weyl semimetals can be considered intermediate phases between different 3D Chern insulators (as shown in Figure 3.7), it is shown in Ref. [29] that class AII semimetals can mediate phase transitions between different strong and weak 3D insulators via Weyl point creation and annihilation.

As discussed in Section 3.1, time reversal symmetry squaring to $T^2 = -1$ forces Weyl points to appear in Kramers pairs of the same chirality, related by $\mathbf{k} \leftrightarrow -\mathbf{k}$ in the Brillouin zone. The topology induced by the presence of these pairs must also respect the symmetry, and as such it cannot be studied by simply moving integration planes freely over the individual Weyl points (as previously shown in Figure 3.5). Indeed, recall from Section 2.4.3 that the insulating \mathbb{Z}_2 invariants must be calculated specifically at the T -invariant planes sitting at $k_{x,y,z} \in \{0, \pm\pi\}$. To study how Kramers pairs affect these invariants, their respective planes must be continuously deformed across them in a way that respects the symmetry, leading to the concept of *curved T-planes*; see Figure 3.9.

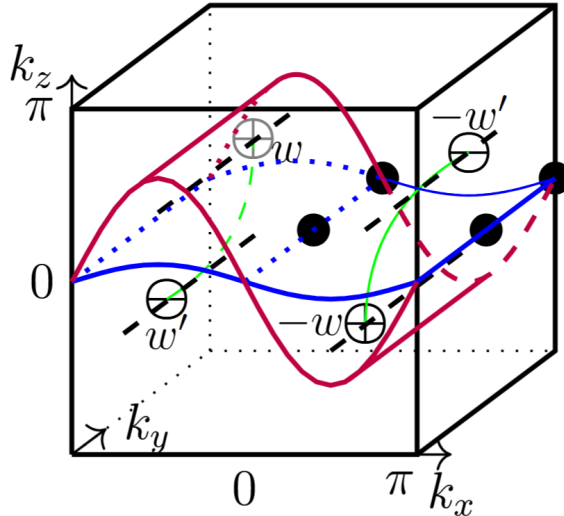


Figure 3.9: Figure from Ref. [29]. Curved T-planes are shown in blue and purple; both are deformations of the $k_z = 0$ plane. Deforming the blue plane into the purple one makes it cross the Kramers pair at $\mathbf{k} = \pm w$. This induces a change in the related \mathbb{Z}_2 invariant: if the Weyl points in this pair have individual charges of q , then the invariants on these planes are related by $\Delta_{z,0}^{\text{purple}} \equiv \Delta_{z,0}^{\text{blue}} + q \pmod{2}$.

The cohomology description must be altered in several ways in order to accommodate this more complex topology. First of all, the cohomology classes must respect the $\mathbf{k} \leftrightarrow -\mathbf{k}$ symmetry on the Brillouin zone, leading to the use of *equivariant* cohomology groups $H_{\mathbb{Z}_2}^n$, where the \mathbb{Z}_2 stands for the \mathbb{Z}_2 action of the symmetry. Mathematically, this is similar in spirit to studying the topology of the *effective Brillouin zone* covering half the torus \mathbb{T}^3 , obtained from the quotient $\mathbb{T}^3/\mathbb{Z}_2$ of the symmetric action. However, the presence of high-symmetry points means some topological information is lost in passing to this effective Brillouin zone, and so a somewhat more involved construction called the *homotopy quotient* must be employed

instead.¹⁹

Secondly, the non-trivial topology existing at the time-reversal invariant momenta (TRIM) necessitates that the cohomology groups be calculated relative to these points. This relative cohomology is defined in much the same way as the relative *homology* featured in Equation (3.9).

Lastly, the cohomology must be *twisted*; that is, it is endowed with *local coefficients* $\tilde{\mathbb{Z}}$, which change sign under the \mathbb{Z}_2 action of the symmetry. We will provide a more geometric intuition behind these local coefficients in Section 4.2.

All in all, the regular cohomology groups in the Mayer–Vietoris sequence in Equation (3.11) must be changed to rather complicated *twisted equivariant* cohomology relative to the TRIM. For example, the insulating invariants (i.e. Chern vectors) in $H^2(\mathbb{T}^3) \cong \mathbb{Z}^3$ are altered to

$$H_{\mathbb{Z}_2}^2(\mathbb{T}^3, \text{TRIM}; \tilde{\mathbb{Z}}) \cong \mathbb{Z}_2^4,$$

containing precisely the four \mathbb{Z}_2 invariants: three weak and one strong. The use of this form of cohomology is motivated in Ref. [29] by the classification of so-called “Quaternionic” vector bundle structures on the Brillouin zone, which are a modification of the usual complex vector bundles induced by the $T^2 = -1$ symmetry [30, 31].

The dual homology picture is considerably simpler in this case. The only modification necessary to the groups in the homology sequence in Equation (3.13) is the use of equivariant homology $H_n^{\mathbb{Z}_2}$; that is, instead of generic Dirac loops and strings, the homology classes must be represented by their *T-stable* variants which respect the $\mathbf{k} \leftrightarrow -\mathbf{k}$ symmetry and avoid the TRIM. Just as in the type A system, this leads to an intuitive description of the associated invariants; see for example Figure 3.10.

Calculated using either homology or cohomology, the semimetal Mayer–Vietoris sequence takes on the following explicit form in a class AII system:

$$0 \rightarrow \mathbb{Z}_2^4 \rightarrow \mathbb{Z}_2^4 \oplus \mathbb{Z}^{r-1} \xrightarrow{\beta} \mathbb{Z}^r \xrightarrow{\Sigma} \mathbb{Z} \rightarrow 0, \quad (3.14)$$

where in this case, r labels the number of Kramers pairs rather than individual Weyl points. Its features are very much analogous to the class A sequence in Equation (3.12): it is essentially obtained by substituting the \mathbb{Z}^3 relating to insulating Chern vectors with a \mathbb{Z}_2^4 indexing the weak and strong invariants. Just as before, the map Σ can be used to deduce Nielsen–Ninomiya charge cancellation, and the semimetal group $\mathbb{Z}_2^4 \oplus \mathbb{Z}^{r-1}$ combines the insulating invariants on the left with a \mathbb{Z}^{r-1} representing the set of allowed Weyl point charge configurations. The main difference from the class A case is that the topology is framed in terms of pairs of Weyl points, and as such the minimum number of Weyl points is four instead of two—as we also covered in the physical setting of Section 3.1.

¹⁹This homotopy quotient is obtained from the *Borel construction*, relying on the fact that there is always a contractible space EG (the total space of the so-called *universal bundle*, in this case S^∞) on which the symmetry group G acts freely. The product space $EG \times \mathbb{T}^3$ is then homotopy equivalent to \mathbb{T}^3 , but the diagonal action has no fixed points. Equivariant cohomology is defined as the cohomology of the quotient space of this action: $H_G^n(\mathbb{T}^3) := H^n(EG \times_G \mathbb{T}^3)$.

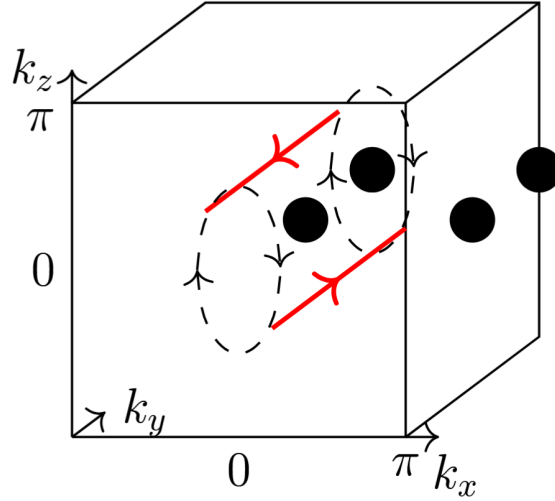


Figure 3.10: Figure from Ref. [29]. A T-stable pair of oriented Dirac loops l_y is shown spanning the k_y direction. The loops may be interchanged while maintaining T-stability, by rotating them along the dashed lines. Doing so recovers the original pair with opposite orientation. It follows that $l_y = -l_y$, that is, $2l_y = 0$; as a result, l_y generates a \mathbb{Z}_2 invariant, dual to the cohomology invariant ν_y .

One might reasonably question whether the classification of Weyl semimetals with additional symmetries always comes down to a mere change in the underlying insulating topology, as it does in this case. In Chapter 4, we will discuss a counterexample to this: we show that the Mayer–Vietoris sequence is altered more radically under a symmetry which has previously been demonstrated to induce novel semimetal topology.

Chapter 4

Non-orientable systems

Symmetries play a crucial role in establishing and differentiating topological properties of physical systems; this is attested by the tenfold way classification discussed in Section 2.3. However, in recent years researchers have begun to recognise that symmetries beyond the standard time reversal, charge conjugation and chiral symmetries can give rise to distinct topological invariants that are not fully captured by this classification.

An important class of these extended symmetries is comprised by the space groups acting on periodic lattices. These impose additional structure on the unit cell of the lattice, such as rotational or reflection symmetry. Of special interest here are the so-called *non-symmorphic* space group symmetries, which combine basic rotation, reflection or inversion with a fractional lattice translation. These symmetries have no fixed points and may induce novel topological states when applied to a material lattice. This type of symmetry has been studied extensively in real space [32–43]; a review can be found at Ref. [44].

Very recently, the feasibility of applying these non-symmorphic symmetries in momentum space has been demonstrated both theoretically and experimentally. This opens up new and interesting avenues of research relating to Brillouin zone topology. In particular, the Brillouin zone may become effectively non-orientable, challenging the notion of chirality for Weyl points.

We begin this chapter with a short review of existing literature surrounding these momentum-space non-symmorphic symmetries, culminating in a treatment of a recent paper which applies them to Weyl semimetals. We then present a novel topological analysis of the system described in this paper, in terms of the cohomology and homology tools presented in Chapter 3.

4.1 Review of recent literature

Non-symmorphic symmetries have been studied somewhat extensively in real space, but their momentum space counterparts have long eluded study. There is a practical reason for this: normally, any space group symmetry in real space gives rise to a symmorphic (i.e. point group) symmetry in momentum space after Fourier transformation, regardless of the nature of the real space symmetry [45]. In order to obtain a non-symmorphic symmetry in momentum space, it is necessary to change how

the real-space symmetry group acts on states in the Hilbert space. The reasoning is as follows: a symmetry group G acts on states in the Hilbert space through a representation ρ . This representation is normally a homomorphism, i.e. it obeys

$$\rho(g)\rho(h) = \rho(gh)$$

for $g, h \in G$. However, since quantum states are physically equivalent up to a U(1) phase, the representation ρ may also include U(1) factors:

$$\rho(g)\rho(h) = \nu(g, h)\rho(gh),$$

where $\nu : G \times G \rightarrow \text{U}(1)$ is known as a factor system [46]. Such a representation is called *projective*, and it may fundamentally alter the algebraic properties of the symmetry group—for example, it can lead symmetry operations that commute in real space to anticommute instead in Hilbert space. Projective representations have previously been studied in more abstract systems, and may give rise to novel topological phases on their own [46–51]. The usual strategy is to implement *gauge fluxes* on the real-space lattice; these are structures that induce U(1) phase changes in particles hopping around the lattice.

The first theoretical realisation of non-symmorphic momentum space symmetries was published by Z. Y. Chen, Shengyuan A. Yang and Y. X. Zhao in 2022 [52]. In their work, the authors take a lattice with a mirror symmetry M_x and perpendicular translation symmetry L_y , and demonstrate how negative hopping amplitudes may be implemented in such a way that the resulting gauge fluxes make M_x and L_y anticommute rather than commute; see Figure 4.1(a). This anticommutation changes how the mirror operator acts in momentum space: denoting the momentum space operators by \hat{M}_x and $\hat{L}_y = e^{ik_y}$ (assuming unit lattice spacing in the real y direction), anticommutation implies

$$\hat{M}_x e^{ik_y} \hat{M}_x = -e^{ik_y} = e^{i(k_y + \pi)}.$$

That is, \hat{M}_x induces not only a mirroring $k_x \mapsto -k_x$, but also a translation by π in the k_y direction. It follows that the momentum-space Hamiltonian must obey the *glide symmetry*

$$U\mathcal{H}(k_x, k_y)U^\dagger = \mathcal{H}(-k_x, k_y + \pi). \quad (4.1)$$

Crucially, the action of this symmetry is free, i.e. there are no high-symmetry momenta that are fixed by \hat{M}_x . Similar to the way in which the free translation symmetries on the 2D lattice reduce momentum space from \mathbb{R}^2 down to the Brillouin torus \mathbb{T}^2 , this free \mathbb{Z}_2 glide symmetry reduces the torus further down to a *fundamental domain* covering half the torus from $k_y = -\pi$ to $k_y = 0$. Whereas the boundary conditions on the full torus are periodic, this fundamental domain features anti-periodic boundary conditions in the k_y direction, in the sense that the $k_y = -\pi$ and $k_y = 0$ boundaries must be identified with opposite orientations. As such, it assumes the topology of the Klein bottle K^2 , which is a non-orientable surface; see Figure 4.1(b).

This glide symmetric system is found to feature a \mathbb{Z}_2 invariant ν , different from the \mathbb{Z} invariant on the 2D Chern insulators discussed in Section 2.4.1. The difference may be explained in terms of cohomology: the regular Chern number is related

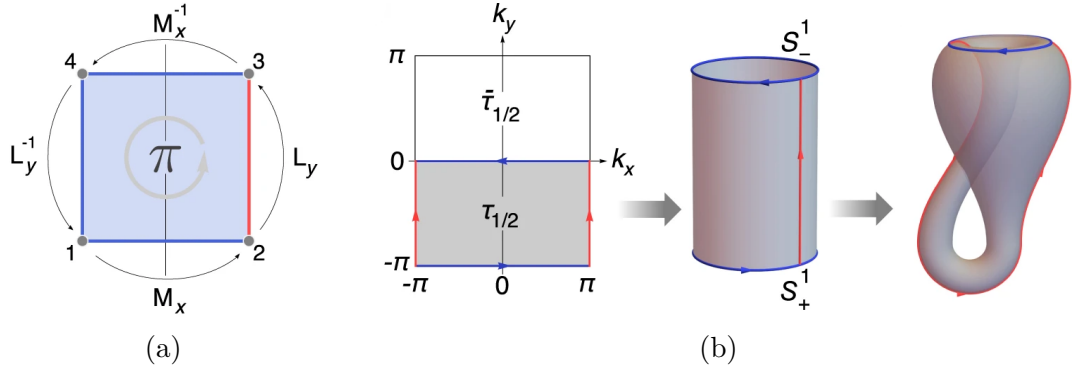


Figure 4.1: Figures adapted from Ref. [52]. (a) A square section of the lattice is shown with a negative hopping amplitude in red. This induces a phase change of π (i.e. a sign change) on a test particle which is moved around the square by successive symmetry operations $L_y^{-1}M_x^{-1}L_yM_x$. The operators M_x and L_y anticommute as a result. (b) The momentum space symmetry \hat{M}_x reduces the Brillouin torus to the fundamental domain shaded in grey on the left. The boundaries of this domain are identified in such a way that it assumes the topology of the Klein bottle K^2 (shown on the right). This surface cannot be given a consistent orientation: one can imagine starting on the outside of the main bulb, entering through the funnel at the top and ending up on the inside.

to $H^2(\mathbb{T}^2) \cong \mathbb{Z}$, whereas in the case of the Klein bottle, the invariant is classified by $H^2(K^2) \cong \mathbb{Z}_2$. This \mathbb{Z}_2 invariant cannot be stated simply in terms of a Berry curvature integral on the fundamental domain: the boundaries at $k_y = -\pi$ and $k_y = 0$ are identified in opposite directions, and their contributions to the integral no longer cancel by Stokes' theorem. Instead, the invariant takes the following two forms in Ref. [52]:

$$\nu \equiv \frac{1}{2\pi} \int_{\tau_{1/2}} \mathcal{F} + \frac{1}{\pi} \gamma(0) \mod 2 \quad (4.2)$$

$$\equiv \frac{1}{2\pi} [\gamma(0) + \gamma(-\pi)] \mod 2, \quad (4.3)$$

where $\tau_{1/2}$ is the fundamental domain and $\gamma(k_y)$ is the Berry phase over the loop at k_y . These two forms are related by Stokes' theorem, and the modulus 2 is necessary to ensure gauge invariance.¹

In 2023, Chen Zhang et al. (including two of the authors of the aforementioned Klein bottle paper) generalised this theoretical framework [45]. In particular, they specify how to obtain all 157 non-symmorphic symmetries in three dimensions (and all four in two dimensions) from real-space gauge symmetries.

Several experimental verifications of these momentum-space non-symmorphic symmetries were published in 2024: Ref. [53] by Yu-Liang Tao, Mou Yan et al. and Ref. [54] by Zhenxiao Zhu et al. In both works, a 3D acoustic lattice is constructed—an artificial crystal in which the band structure is represented by frequencies of

¹Note that in the latter equation, it is important that $\gamma(0)$ and $\gamma(-\pi)$ are both calculated in the same gauge, which must be continuous across the fundamental domain $\tau_{1/2}$.

sound waves—featuring negative hopping amplitudes, which induce non-symmorphic symmetries in momentum space; see Figure 4.2. These symmetries are shown to give

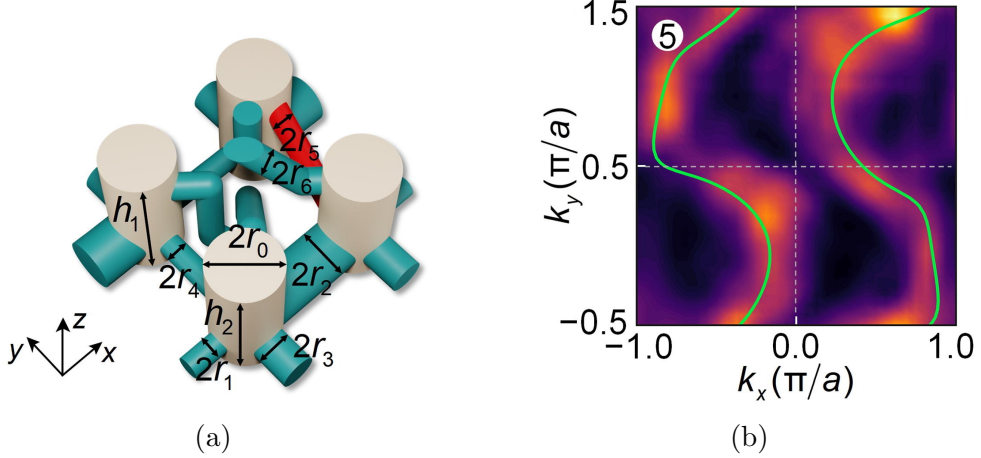


Figure 4.2: Figure adapted from Ref. [54]. (a) Unit cell of the acoustic crystal used in the experiment. The resonant cavities shown in beige approximate tight-binding orbitals in electronic systems, while the coupling tubes in green simulate hopping between lattice sites. The tube indicated in red has an effective negative hopping amplitude. (b) Experimental (colour map) and numeric (green) data from a 2D slice of the system’s Brillouin zone. The figure shows the response to a specific frequency, equivalent to an equal-energy contour (i.e. section of the bands) in an electronic system. This 2D slice features a glide symmetry: the lower half can be obtained by mirroring the upper half in the horizontal k_x direction.

rise to novel topological phases and surface behaviour.

Several other works have explored a specific non-symmorphic symmetry group in two dimensions, where besides the glide symmetry \hat{M}_x giving rise to Equation (4.1), there is also a perpendicular glide symmetry \hat{M}_y in which the roles of k_x and k_y are reversed [55–57]. This double glide symmetry is notable in that, even though the action of each individual glide symmetry \hat{M}_x and \hat{M}_y on the Brillouin torus is free, the combined action of the two is not. Instead, there are four high-symmetry momenta² at $\mathbf{k} = (\pm\pi/2, \pm\pi/2)$ which are fixed under $\hat{M}_y\hat{M}_x$; see Figure 4.3. It is noted in Refs. [55] and [56] that a \mathbb{Z}_2 topological invariant can be calculated based on the eigenvalues of $\hat{M}_x\hat{M}_y$ at these high-symmetry points, similar to the \mathbb{Z}_2 invariants in the time-reversal invariant systems encountered in Section 2.4.

4.1.1 Non-orientable Weyl semimetals

The first work in which non-symmorphic symmetries were explored in the context of Weyl semimetals was a 2024 paper by André Grossi Fonseca, Sachin Vaidya et al. [7]. The remainder of this section is dedicated to summarizing the main findings in this paper.

²In crystallographic terms, the 2D wallpaper group Pgg has four special Wyckoff positions.

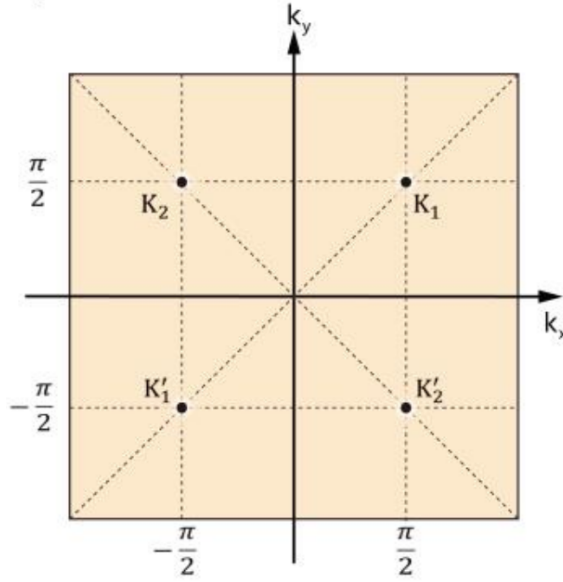


Figure 4.3: Figure from Ref. [56]. The points labelled K_a with $a \in \{1, 2\}$ are related by either single glide symmetry to those labelled K'_a respectively. As a result, applying both symmetries at once fixes all four of these points. The four indicated dashed lines are also fixed sets of the combined symmetry.

The basic setup in Ref. [7] is that of an abstract 3D Brillouin torus featuring a glide symmetry of the form

$$\mathcal{H}(k_x, k_y, k_z) = \mathcal{H}(-k_x, k_y + \pi, k_z); \quad (4.4)$$

no assumptions are made on the source of this symmetry.³ The free action of this symmetry gives rise to a non-orientable fundamental domain: slices of constant k_z take on the topology of the Klein bottle K^2 in the same way as in Ref. [52] discussed above. Taking into account the additional periodic k_z direction, the total fundamental domain is topologically the non-orientable manifold $K^2 \times S^1$; see Figure 4.4. In Ref. [7], the fundamental domain is taken to be the half torus with $k_y \leq 0$, with additional boundary identifications between the planes $k_y = -\pi$ and $k_y = 0$ which respect the symmetry.

The non-orientability of the fundamental domain is shown to lead to some novel properties. Most notably, the chirality of Weyl points is no longer well-defined in a non-orientable setting: for example, when a Weyl point which has a Chern number of -1 leaves the fundamental domain at the $k_y = -\pi$ plane, it returns at the corresponding point on the $k_y = 0$ plane with a Chern number of $+1$. Physically, this is because the glide symmetry in Equation (4.4) is parity-reversing, which induces a sign change in the Berry curvature.

These chirality changes may result in a system in which the total chirality of Weyl points does not add to zero on the fundamental domain; that is, the Nielsen–Ninomiya

³The symmetry is presented without unitary conjugation, but as noted in the supplement to Ref. [7], the presence of such a conjugation [as in Equation (4.1)] makes no difference topologically.

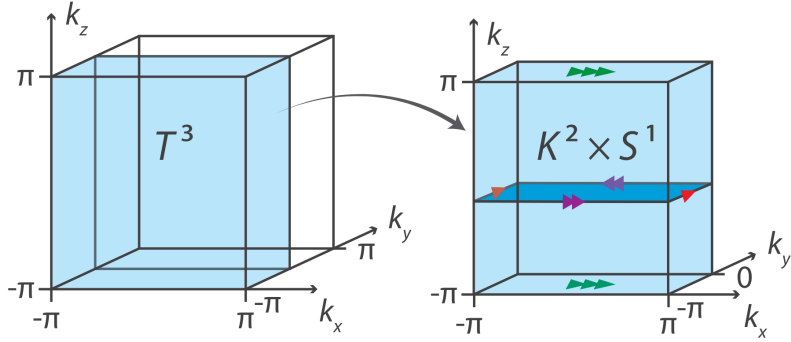


Figure 4.4: Figure adapted from Ref. [7]. The glide symmetry in Equation (4.4) acts on the Brillouin torus \mathbb{T}^3 in such a way that the fundamental domain (covering half the torus) is topologically $K^2 \times S^1$. Coloured arrows indicate the correct boundary identifications.

charge cancellation theorem in Equation (3.7) is circumvented. In particular, two Weyl points with the same chirality may be connected by a Fermi arc on an xy -like surface, see Figure 4.5. It is demonstrated that a Fermi arc on such a surface connects

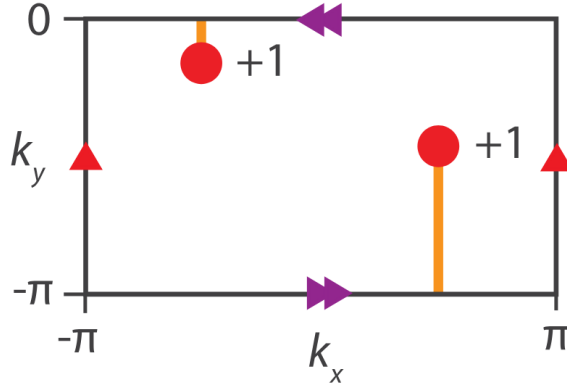


Figure 4.5: Figure from Ref. [7]. Surface Brillouin zone obtained from imposing open boundary conditions in the z direction. A Fermi arc is shown which connects (projections of) Weyl points of the same chirality. This Fermi arc crosses the orientation-reversing boundary at $k_y = 0$ once (i.e. an odd number of times).

two same-chirality Weyl points if and only if it lies on an “orientation-reversing path”, i.e. it crosses the line at $k_y = 0$ an odd number of times.

Moreover, a new charge cancellation theorem is derived from a \mathbb{Z}_2 invariant ν existing on gapped K^2 -like slices of constant k_z . This invariant is equivalent to that on the Klein bottle insulator in Ref. [52], and is calculated using Equations (4.2) and (4.3). It is shown that this invariant changes whenever such a slice is moved across a Weyl point of odd chirality in the k_z direction, see Figure 4.6. It is then argued that, since the fundamental domain is periodic in the k_z direction, there must be an even number of such changes in ν . This leads to a novel \mathbb{Z}_2 charge cancellation condition for Weyl points on $K^2 \times S^1$: if there are k Weyl points $w_i \in W$, then their Chern

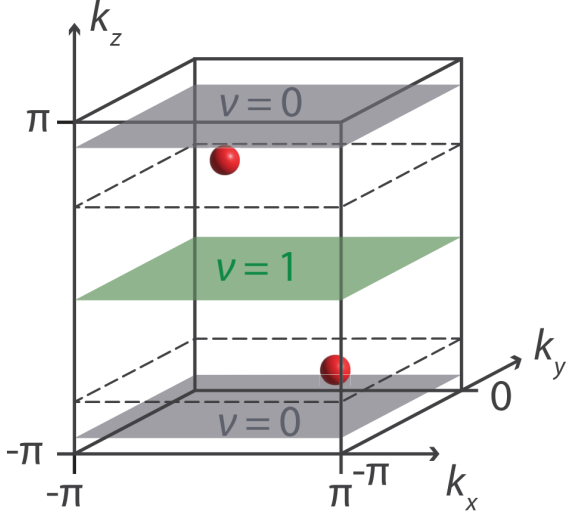


Figure 4.6: Figure from Ref. [7]. The $K^2 \times S^1$ fundamental domain is shown featuring two Weyl points, both with chirality +1. The invariant ν is shown to vary in the k_z direction, depending on the presence of Weyl points. Periodicity in the k_z direction then dictates that the total parity of the Weyl points must be even.

numbers C_{w_i} must obey

$$\sum_{i=1}^k C_{w_i} = 0 \pmod{2}. \quad (4.5)$$

Finally, an experimental realisation of a Weyl semimetal with momentum-space glide symmetry is provided. One-dimensional photonic crystals are used to represent the k_z direction, and the k_x and k_y directions are represented synthetically by using samples with different optical properties. In this way, a Fermi arc is demonstrated which terminates in two points of similar chiralities.

[Even if I end up not discussing non-Hermitian systems, the König, Yang et al. preprint [58] should probably get at least an honourable mention. I'll decide on the extent of coverage closer to the deadline.]

4.2 Topological exploration

The purpose of this section is to reframe and analyse the non-orientable Weyl semimetals described in Ref. [7] in terms of the algebraic topology language from Chapter 3. This approach has the advantage of being coordinate-free, and as such it provides a more fundamental understanding of the system's topological properties. We obtain a direct description of how the Nielsen–Ninomiya theorem is modified into the \mathbb{Z}_2 charge cancellation condition in Equation (4.5). We also obtain a more complete picture of the different invariants associated with such a system, and are able to distinguish which are related to the topological insulator phase, and which relate to the introduction of Weyl nodes. To the knowledge of the author, the insights contained in this section are novel.

4.2.1 Preliminary clarifications

As a motivation for the proposed coordinate-free description, we begin by clarifying some minor points of confusion present in Ref. [7].

First of all, there is a relatively strong emphasis on the two “orientation-reversing planes” at $k_y = \pm\pi$ and $k_y = 0$. For example, it is stated that relative chirality can be defined unambiguously on fundamental domains that avoid these planes. This is true on a technical level, but it creates the impression that the orientation reversal occurs locally at the boundary of the fundamental domain, raising questions about the nature of Weyl points existing on these planes.

In reality, orientation reversal is a global feature. We are free to reparametrise the fundamental domain in a way that includes the planes $k_y = \pm\pi$ and $k_y = 0$, and the notion of relative chirality may change as a result; this is illustrated in Figure 4.7. For any given set of distinct Weyl points obeying the symmetry, it is possible in

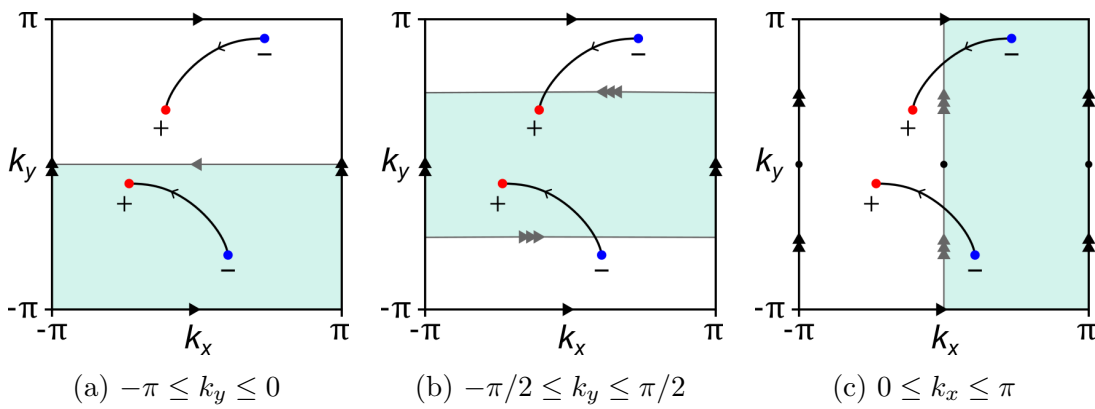


Figure 4.7: Top view of the 3D Brillouin torus (or 2D surface torus) for a given Weyl semimetal state obeying the glide symmetry in Equation (4.4), with Weyl points and oriented Dirac strings (Fermi arcs) drawn in. Different parametrisations of the fundamental domain are shaded in teal: (a) the domain outlined in Ref. [7]; (b) the same domain shifted in the k_y direction; (c) a domain spanning the k_y direction. Each of these domains is homeomorphic to $K^2 \times S^1$ (K^2) under the boundary identifications shown. Note that both the absolute and relative chirality of the two Weyl nodes in the fundamental domain change under these alternative parametrisations.

principle to achieve any relative chirality by reparametrising the fundamental domain. It should be noted that there do exist two planes that are of special significance, namely the so-called *glide planes* at $k_x = 0$ and $k_x = \pm\pi$; these planes are (taken as a whole) invariant under the symmetry, and as such they cannot be excluded completely from any given parametrisation.

A similar point of confusion arises in explaining how the usual relation between Nielsen–Ninomiya and the Poincaré–Hopf theorem for vector fields breaks down. On the regular Brillouin torus, the factor $\mathbf{h}(\mathbf{k})$ in the Bloch Hamiltonian can be considered a continuous vector field tangent to the torus. The Poincaré–Hopf theorem then tells us that the zeroes of such vector fields must have topological indices (corresponding

to Weyl point chiralities) adding up to zero.

In the supplement to Ref. [7], the failure of Poincaré–Hopf is attributed to a discontinuity of the vector field at the planes $k_y = \pm\pi$ and $k_y = 0$; see Figure 4.8. However, this mischaracterises the situation somewhat; in reality, $\mathbf{h}(\mathbf{k})$ cannot be

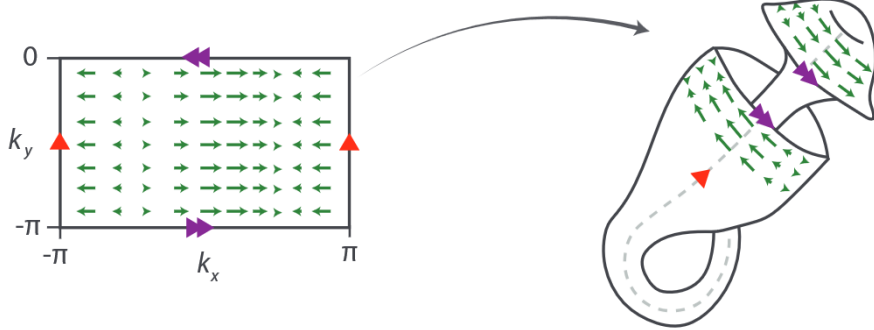


Figure 4.8: Figure from the supplement to Ref. [7]. The k_x component of an example $\mathbf{h}(\mathbf{k})$ is mapped onto a K^2 slice of the fundamental Brillouin zone and then “bent into shape” to demonstrate discontinuity.

considered a well defined tangent vector field to $K^2 \times S^1$ to begin with. This is illustrated in Figure 4.9: two vectors which point away from each other in the fundamental domain may instead point towards each other after applying the glide symmetry. As such, \mathbf{h} should be thought of as a more abstract map $K^2 \times S^1 \rightarrow \mathbb{R}^3$

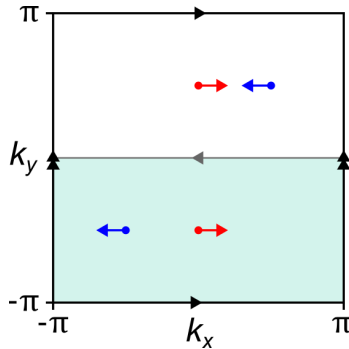


Figure 4.9: Example vectors $\mathbf{h}(\mathbf{k})$ on the glide symmetric Brillouin zone. Similar colours indicate that the vectors are related by glide symmetry.

rather than a tangent vector field, and Poincaré–Hopf does not apply to such maps.⁴

It is worth emphasizing that this disconnection from Poincaré–Hopf is a general feature of non-orientable manifolds, not one that is specific to the model Hamiltonian. Smooth tangent vector fields can in fact be defined on $K^2 \times S^1$, but a Hamiltonian cannot be associated to them in a canonical way. Such a construction usually requires using gamma matrices that “twist along” with the tangent bundle of the manifold instead of the regular vector of Pauli matrices, but these gamma matrices cannot

⁴To be precise, \mathbf{h} is a section of the trivial \mathbb{R}^3 -bundle over $K^2 \times S^1$, not of its tangent bundle. In the usual case of the torus, these descriptions are equivalent: \mathbb{T}^3 is parallelisable, i.e. $T\mathbb{T}^3 \cong \mathbb{T}^3 \times \mathbb{R}^3$. This is what allows Poincaré–Hopf to apply.

be defined consistently on a non-orientable manifold.⁵ As a result, the notion of a tangent vector field loses some of its utility in studying the topological properties of a non-orientable system. Instead, any topological analysis must be performed in terms of more fundamental algebraic topology tools, such as the homology and cohomology relied on in this work.

- This may have very important implications for physical interpretation; for example, it may not be possible to define an effective field theory with an explicit chiral anomaly based on the tangent vector field. Even if the Hamiltonian is constructed as this map $K^2 \times S^1 \rightarrow \mathbb{R}^3$, explicit calculations still rely on writing down coordinates for $\mathbf{k} \in K^2 \times S^1$ —but $K^2 \times S^1$ cannot be covered in a single coordinate chart. Choosing coordinates comes down to this choice of fundamental domain in \mathbb{R}^3 again, which means any possible anomalous features will not be robust under change of coordinates (i.e. not physical).

A final point that merits clarification is the inclusion of a second glide symmetry. The supplement to Ref. [7] discusses imposing Equation (4.4) together with a similar symmetry along the glide plane $k_y = 0$:

$$H(k_x, k_y, k_z) = H(k_x + \pi, -k_y, k_z). \quad (4.6)$$

It is claimed that this double symmetry subdivides the 3-torus into four copies of a different non-orientable manifold $\mathbb{R}P^2 \times S^1$. Here $\mathbb{R}P^2$ is the real projective plane, i.e. the space of all lines through the origin in \mathbb{R}^3 ; it can be obtained by identifying all antipodal points on a 2-sphere. In this case, $\mathbb{R}P^2 \times S^1$ is obtained by imposing anti-periodic boundary conditions in both the k_x and k_y directions on a quarter of the Brillouin zone. However, this direct identification with $\mathbb{R}P^2 \times S^1$ cannot be made as straightforwardly as in the case of a single glide symmetry. As discussed in our review of Refs. [55] and [56], the combination of two perpendicular glide symmetries in two dimensions does not have a free action, leading to the fixed points shown in Figure 4.3.

The situation is analogous in three dimensions: the four lines at the momenta $\mathbf{k} = (\pm\pi/2, \pm\pi/2, k_z)$ are fixed under application of both glide symmetries at once. As a result, a Weyl point existing on one of these lines must have an even chirality, and it only has one symmetric partner in the 3-torus rather than the three one would expect from four identical copies of $\mathbb{R}P^2 \times S^1$.⁶ Such Weyl points are physically

⁵The proper construction is that of a Clifford algebra bundle over the tangent bundle, see Section 4.2 of Ref. [23]. This construction relies on the existence of a spin^c structure on the base manifold, but non-orientable manifolds do not admit such a structure. [The non-existence of a spin^c structure might also have implications for how “physical” a non-orientable BZ really is—I think we may not be able to interpret the Weyl points on as Weyl fermion modes on $K^2 \times S^1$, for example. However, there are modified non-orientable analogues of spin structures (Pin^\pm and pin^c structures) that may be somehow applicable here.]

⁶One can also argue that this must be the case topologically: if a manifold M has an n -sheeted cover \tilde{M} , then the Euler characteristics of both spaces must be related by $\chi(\tilde{M}) = n\chi(M)$. Reducing the system down to two dimensions, we find $\chi(\mathbb{T}^2) = 0$ and $\chi(\mathbb{R}P^2) = 1$, so that the former cannot cover the latter. Instead, the only possible covering space for $\mathbb{R}P^2$ is the double cover $S^2 \rightarrow \mathbb{R}P^2$, since $\chi(S^2) = 2$. Technically speaking, this means the fundamental domain needs to be described as an *orbifold* rather than a manifold, i.e. a space that encodes data about orbits of a group action. For example, the Euler characteristic of $\mathbb{R}P^2$ is zero as an orbifold.

fine-tuned and are expected to split into pairs under perturbations. Nevertheless, additional symmetries may exist which force Weyl points to exist on these lines, in which case the exceptional behaviour becomes key to the description. Moreover, the reduction to a fundamental domain is predicated on a free group action in the main text of Ref. [7]. As such, analysis of a purely $\mathbb{R}P^2 \times S^1$ Brillouin zone cannot a priori be expected to provide the correct topological classification for this double glide symmetry. Indeed, similar to the case of time reversal in Section 3.2.4, a proper classification scheme should involve equivariant cohomology on the torus, bearing in mind the topological role of the high-symmetry points. This becomes manifestly clear from the existence of a topological invariant at these high-symmetry points [55, 56]. This full analysis is somewhat beyond the scope of the present text, and in what follows we will restrict our attention to the case of a single glide symmetry.

4.2.2 Classification scheme

There are two main conceptual challenges that present themselves in attempting to apply consistent cohomology and homology frameworks to non-orientable systems, and in particular in developing a physical intuition for them. First of all, the analogy between second cohomology classes and differential two-forms such as the Berry curvature \mathcal{F} breaks down in this case, and a statement like Equation (3.4) can no longer be taken to hold directly. This is because differential forms like \mathcal{F} cannot be integrated over non-orientable manifolds, and the associated (de Rham) cohomology group is actually real-valued—it cannot readily encode the \mathbb{Z}_2 invariants induced by changes in orientation. As an example, suppose we are trying to find an invariant for the 2D Klein bottle insulator obeying Equation (4.1). Integrating a Berry curvature on K^2 directly is not well defined, while integrating over the entire Brillouin torus always yields zero: the integration is over two oppositely oriented areas. The correct \mathbb{Z}_2 invariant can be interpreted as integration with different signs on both halves of the torus, bearing in mind that the result is only gauge invariant mod 2. In order to capture this behaviour generally, we need to move to the richer but more abstract integer-valued cohomology. [Probably add a reference to the (co)homology appendix here.]

The second obstacle is that Poincaré duality is altered in this context. In Section 3.2, this form of duality was used to identify the familiar cohomology invariants with homology invariants, in the form of non-trivial oriented loops and Dirac strings. In a non-orientable system, this identification cannot be made directly; in this case, either the homology or the cohomology must be *twisted* by the introduction of a *local coefficient system* $\tilde{\mathbb{Z}}$ [28, 59]. Such a coefficient system compensates for the twist in orientation by tracking sign changes across the manifold. Introducing local coefficients on an n -manifold M gives rise to the twisted homology and cohomology groups $H_k(M; \tilde{\mathbb{Z}})$ and $H^k(M; \tilde{\mathbb{Z}})$. Poincaré duality then takes the following forms [28, Theorem 3H.6]:

$$\begin{aligned} H_k(M; \tilde{\mathbb{Z}}) &\cong H^{n-k}(M), \\ H^k(M; \tilde{\mathbb{Z}}) &\cong H_{n-k}(M). \end{aligned}$$

That is, twisting either one of the homology or cohomology restores Poincaré duality;

if the homology is twisted, ordinary cohomology must be used and vice versa. When M is orientable, the local coefficients become trivial and the original form of Poincaré duality is recovered from both relations.

Given the fact that Poincaré duality can be restored by twisting either the homology or the cohomology group, the correct classification of a non-orientable physical system hinges on this choice of twist. Fortunately, there is a straightforward way to decide between the two in the case of a Weyl semimetal with an orientation-reversing \mathbb{Z}_2 symmetry. In this situation, Poincaré duality is necessary in order to relate the chirality of Weyl points (which are cohomology invariants) to the orientation of their corresponding Dirac strings (which are the dual homology invariants). Under the orientation-reversing symmetry, Poincaré duality breaking manifests itself in the fact that the Weyl point chiralities are naturally reversed, while the orientation of Dirac strings is unchanged. This is illustrated schematically in Figure 4.10. The

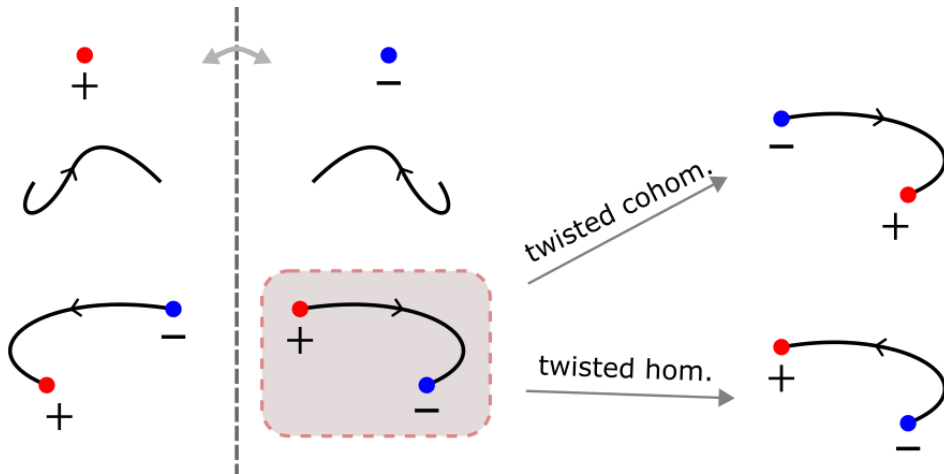


Figure 4.10: On the top left, the action of an orientation-reversing symmetry (represented by the dashed mirror axis) is shown on a Weyl point [whose chirality is an invariant in $H^2(M \setminus W)$] and a Dirac string [representing an invariant in $H_1(M, W)$]. The Weyl point has its chirality reversed, since the Chern number is a pseudoscalar. On the other hand, the Dirac string is mirrored but maintains its internal orientation (i.e. its image is also oriented away from the “hook” at the end). As a result, when the symmetry acts on a set of two Weyl points connected by a Dirac string, the resulting structure has a Dirac string whose orientation is inconsistent with the chirality of the Weyl points (shown in the shaded area)—this is a result of Poincaré duality breaking. This problem can be resolved in one of two ways: either the cohomology is twisted into $H^2(M \setminus W; \widetilde{\mathbb{Z}})$ to undo the chirality reversal, or the homology is twisted into $H_1(M, W; \widetilde{\mathbb{Z}})$ to reverse the Dirac string’s orientation. Poincaré duality is restored in both cases; the correct approach depends on the physical setup.

decision of which group must be twisted can thus be made by noting how the chirality of Weyl points (outside of high-symmetry points) relates to that of their symmetric partners in the full Brillouin torus. To be precise, the presence of same-chirality pairs indicates that the (cohomological) Chern number is not reversed as expected,

and the cohomology must be twisted. Meanwhile, pairs with opposite chiralities indicate that the cohomology behaves naturally, and the homology (i.e. the Dirac string orientations) must be twisted to follow suit.

[The next few paragraphs are subject to change, the maths don't quite work out – e.g. the sign of T^2 appears to be relevant as well. Their contents do not influence the logic in the later paragraphs in any significant way.] Physically, this twisting of the homology may be related to the unitarity or anti-unitarity of the symmetry operation. This can be seen as follows: in the case of a unitary symmetry relating $\mathbf{k} \leftrightarrow \mathbf{k}'$, the Hamiltonian obeys

$$U\mathcal{H}(\mathbf{k})U^\dagger = \mathcal{H}(\mathbf{k}').$$

If $|\psi(\mathbf{k})\rangle$ is an eigenstate of $\mathcal{H}(\mathbf{k})$, it follows that $|\psi(\mathbf{k}')\rangle := U|\psi(\mathbf{k})\rangle$ is an eigenstate of $\mathcal{H}(\mathbf{k}')$, and so the Berry connection transforms as

$$\begin{aligned}\mathcal{A}(\mathbf{k}) &= i\langle\psi(\mathbf{k})|\partial_{\mathbf{k}}\psi(\mathbf{k})\rangle \cdot d\mathbf{k} \\ &= i\langle\psi(\mathbf{k}')|UU^\dagger|\partial_{\mathbf{k}}\psi(\mathbf{k}')\rangle \cdot d\mathbf{k} \\ &= i\langle\psi(\mathbf{k}')|\partial_{\mathbf{k}'}\psi(\mathbf{k}')\rangle \cdot d\mathbf{k}' \quad \downarrow UU^\dagger = 1, \partial_{\mathbf{k}}f \cdot d\mathbf{k} = \partial_{\mathbf{k}'}f \cdot d\mathbf{k}' \\ &= \mathcal{A}(\mathbf{k}').\end{aligned}$$

Since the Berry connection one-form is left invariant, so is the Berry curvature two-form. A final minus sign is then induced by the change of orientation when integrating this two-form, so that the Chern number (Weyl point chirality) changes sign under unitary orientation-reversing symmetries. This is exactly what is implied when the Chern number is called a pseudoscalar. Looking back at Figure 4.10, twisted homology (and its dual ordinary cohomology) must be used to obtain the correct invariants.

On the other hand, under an anti-unitary symmetry the Hamiltonian transforms as [for $T^2 = -1$]

$$U\mathcal{H}(\mathbf{k})U^\dagger = \mathcal{H}^*(\mathbf{k}'),$$

and its eigenstates obey $\langle\psi(\mathbf{k}')| = U|\psi(\mathbf{k})\rangle$. The unitary matrix U drops out of the Berry connection as before, and we are left with

$$\begin{aligned}\mathcal{A}(\mathbf{k}) &= i\langle\psi(\mathbf{k})|\partial_{\mathbf{k}}\psi(\mathbf{k})\rangle \cdot d\mathbf{k} \\ &= i\langle\partial_{\mathbf{k}'}\psi(\mathbf{k}')|\psi(\mathbf{k}')\rangle \cdot d\mathbf{k}' \\ &= -(i\langle\psi(\mathbf{k}')|\partial_{\mathbf{k}'}\psi(\mathbf{k}')\rangle)^* \cdot d\mathbf{k}' \\ &= -\mathcal{A}^*(\mathbf{k}') = -\mathcal{A}(\mathbf{k}),\end{aligned}$$

where the last equality holds because \mathcal{A} is a real-valued one-form. It follows that the Berry curvature and its associated Chern numbers pick up an additional minus sign, which cancels out the orientation reversal. As a result, Weyl points have the same sign as their symmetric partners, and the correct description is given by twisted cohomology and ordinary homology.

As an example, we may apply this line of reasoning to the time reversal invariant Weyl semimetal from Section 3.2.4. This system is not usually thought of in terms of non-orientability, but the time reversal symmetry acts in an orientation-reversing

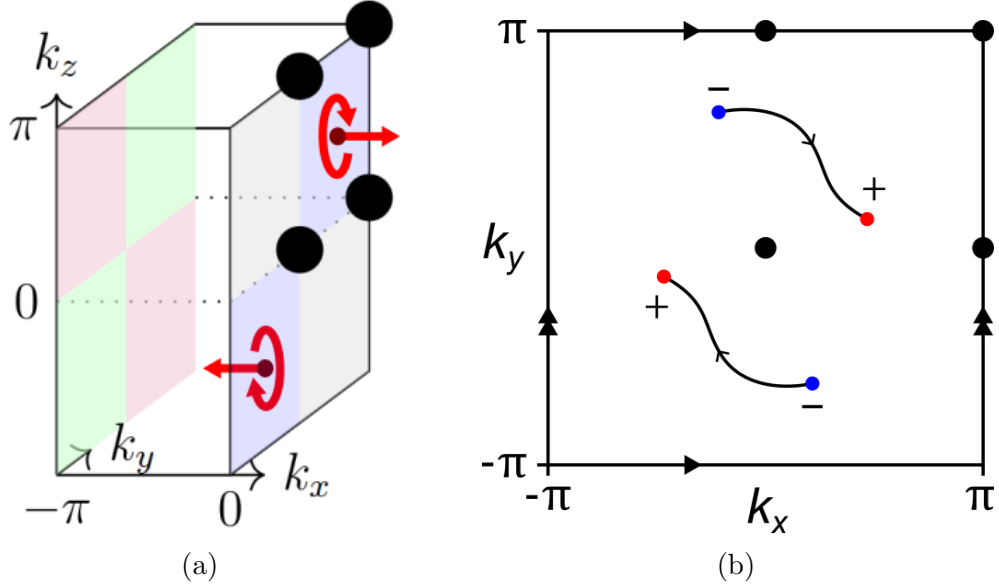


Figure 4.11: (a) Figure adapted from Ref. [29]. The effective Brillouin zone under time reversal symmetry is half of \mathbb{T}^3 , with additional identifications of the coloured areas as $k \sim -k$. The resulting space is non-orientable: a “test particle” with a given helicity is shown travelling out through the boundary at $\mathbf{k} = (0, \pi/2, \pi/2)^T$, and reappearing at $\mathbf{k} = (0, -\pi/2, -\pi/2)^T$ with the opposite helicity. (b) Top view of a time reversal invariant Weyl semimetal, featuring same-chirality Kramers pairs at conjugate momenta, indicating a twist in the cohomology. On the other hand, the orientation of Dirac strings respects the symmetry, indicating ordinary (“untwisted”) homology.

way: an odd number (i.e. all three) of momentum directions are inverted, leading to a change of parity. Figure 4.11(a) illustrates that the effective Brillouin zone is indeed non-orientable. As discussed before, **the time-reversal symmetry in this system is anti-unitary, and as such** the Kramers pairs of Weyl points at opposite momenta (related by $\mathbf{k} \leftrightarrow -\mathbf{k}$) always have the same chirality; see Figure 4.11(b). Again, these same-chirality pairs are an indication that the Chern numbers of Weyl points do not transform as expected, and so the cohomology must be twisted. It follows that the homology should not be twisted; this can also be seen directly from the Dirac strings in Figure 4.11(b), whose orientation is directly related by the symmetry (i.e. the arrows run in relative directions respecting $\mathbf{k} \leftrightarrow -\mathbf{k}$). This description in terms of twisted cohomology and ordinary homology agrees exactly with the one given in Section 3.2.4, which was derived from more abstract vector bundle classification arguments in Ref. [29]. In this particular case, direct calculation of the (co)homology groups on the effective Brillouin zone is complicated by the existence of high-symmetry points (i.e. the action of the symmetry is not free), which is why the authors of Ref. [29] use equivariant (co)homology on the full torus.

Returning to the case of a momentum-space glide symmetry, we can see from Figure 4.7(a) that the situation is different here. **The unitary nature of the symmetry means that** every Weyl point in the fundamental domain is related by symmetry

to an oppositely charged point in the other half of the torus, while the orientation of Dirac strings is reversed under the symmetry. It follows that the classification of topological phases should rely on twisted *homology*, and equivalently, ordinary cohomology. Since there is a proper fundamental domain in this case, there is no need to compute equivariant (co)homology groups, and we may instead rely on ordinary cohomology and twisted homology on $K^2 \times S^1$.⁷

The choice of ordinary cohomology can be corroborated in two important ways. Firstly, the use of ordinary second cohomology classes indicates that we are classifying complex line bundles over the fundamental domain. An important insight from K-theory tells us that this is equivalent to classifying equivariant line bundles over the full torus [61, Proposition 2.1].⁸ That is, we are classifying states that respect the symmetry directly. Secondly, the \mathbb{Z}_2 invariant found in Ref. [7] on K^2 -like slices of constant k_z is recovered using ordinary cohomology, related to the fact that $H^2(K^2) \cong \mathbb{Z}_2$. Twisted cohomology would give a $H^2(K^2; \mathbb{Z}) \cong \mathbb{Z}$ invariant on these slices.

All in all, we find that the correct classification of semimetal phases in this system is given by the following Mayer–Vietoris exact sequence of cohomology groups on $M := K^2 \times S^1$:

$$0 \rightarrow \underbrace{H^2(M)}_{\text{Insulator}} \rightarrow \underbrace{H^2(M \setminus W)}_{\text{Semimetal}} \rightarrow H^2\left(\bigcup_{i=1}^k S_{w_i}^2\right) \xrightarrow{\Sigma} H^3(M) \rightarrow 0, \quad (4.7)$$

where as before, W is the set of Weyl points on M and $S_{w_i}^2$ is a small 2-sphere surrounding the Weyl point $w_i \in W$. Equivalently, the classification may be given in terms of the following dual *twisted* homology sequence:

$$0 \rightarrow \underbrace{H_1(M; \widetilde{\mathbb{Z}})}_{\text{Twisted Dirac loops}} \rightarrow \underbrace{H_1(M, W; \widetilde{\mathbb{Z}})}_{\text{Twisted Dirac strings}} \xrightarrow{\partial} H_0(W; \widetilde{\mathbb{Z}}) \xrightarrow{\Sigma} H_0(M; \widetilde{\mathbb{Z}}) \rightarrow 0, \quad (4.8)$$

where we refer to the Dirac loops and Dirac strings as twisted to emphasise the non-trivial action of the symmetry on their orientation. The concept of a twisted Dirac string on $K^2 \times S^1$ can be difficult to intuit, leading to Dirac strings that appear to change orientation at orientation-reversing boundaries of the fundamental domain in a setup like Figure 4.7(c). As such, they are more readily understood as equivariant (i.e. symmetry-related) pairs of Dirac strings on the full torus \mathbb{T}^3 , whose orientation is reversed under the symmetry.

In what follows, we will provide explicit computations of these sequences and discuss the associated invariants.

4.2.3 Computation of invariants on $K^2 \times S^1$

The use of ordinary cohomology groups in the Mayer–Vietoris sequence (4.7) means that calculations are relatively straightforward, and standard techniques such as

⁷ Formally speaking, equivariant cohomology of a space M with a free action of the group G is equivalent to ordinary cohomology on the quotient space M/G [60, Corollary 9.6].

⁸This is related to footnote 7 in the sense that K-theory is a *generalised cohomology* theory.

cellular cohomology can be applied. [Given enough time, I can include a small Appendix B containing an example cellular cohomology calculation.] Using these methods, we calculate the sequence to be

$$0 \rightarrow \mathbb{Z} \oplus \mathbb{Z}_2 \xrightarrow{\alpha} \mathbb{Z} \oplus \mathbb{Z}_2 \oplus \mathbb{Z}^k \xrightarrow{\beta} \mathbb{Z}^k \xrightarrow{\Sigma} \mathbb{Z}_2 \rightarrow 0, \quad (4.9)$$

where $k = |W|$ is the number of Weyl points. Given that the twisted homology sequence (4.8) is related to the Mayer–Vietoris sequence by Poincaré duality, it features the exact same groups in the same order; the difference is only in the interpretation.

For comparison, we recall here the semimetal Mayer–Vietoris sequence on \mathbb{T}^3 from Section 3.2.3:

$$0 \rightarrow \mathbb{Z}^3 \rightarrow \mathbb{Z}^3 \oplus \mathbb{Z}^{k-1} \xrightarrow{\beta} \mathbb{Z}^k \xrightarrow{\Sigma} \mathbb{Z} \rightarrow 0. \quad (4.10)$$

Some relevant differences between these two sequences are highlighted below.

Insulating phases

The first difference between the Mayer–Vietoris sequences on \mathbb{T}^3 and $K^2 \times S^1$ lies in the insulating topology of the system, in the absence of any Weyl points. Whereas the 3D Chern insulator on the plain torus features a Chern vector in $H^2(\mathbb{T}^3) \cong \mathbb{Z}^3$, this group is reduced to $H^2(K^2 \times S^1) \cong \mathbb{Z} \oplus \mathbb{Z}_2$ under the action of the glide symmetry. As a result, the $K^2 \times S^1$ insulator is not classified by three Chern numbers $C_{x,y,z} \in \mathbb{Z}$, but by a \mathbb{Z} invariant ν_x and a \mathbb{Z}_2 invariant ν_z —the reasoning behind our choice of symbols will become apparent shortly.

The reduction to two invariants can be most readily understood from the twisted homology point of view. On \mathbb{T}^3 , the three generators of $H_1(\mathbb{T}^3) \cong \mathbb{Z}^3$ are represented by oriented Dirac loops $\ell_{x,y,z}$ that wind around the 3-torus once in each respective coordinate direction. Under glide symmetry, each of these loops obtains a symmetric partner $\ell'_{x,y,z}$ with a reversed internal orientation—this is due to the twist in the homology. Taken together with the original loop, $\ell_{x,y,z} + \ell'_{x,y,z}$ is equivalent to a twisted Dirac loop $\tilde{\ell}_{x,y,z}$ on $K^2 \times S^1$, representing an invariant in $H_1(K^2 \times S^1; \widetilde{\mathbb{Z}})$. The reduction to $\mathbb{Z} \oplus \mathbb{Z}_2$ is then caused by specific degeneracies in these twisted Dirac strings: $\tilde{\ell}_x$ generates the full \mathbb{Z} invariant ν_x , $\tilde{\ell}_y$ turns out to be trivial, and $\tilde{\ell}_z$ generates the \mathbb{Z}_2 invariant ν_z . This is illustrated in more detail in Figure 4.12.

The invariant $\nu_z \in \mathbb{Z}_2$ corresponds precisely to the \mathbb{Z}_2 invariant on K^2 slices described in Ref. [7], and stems from the 2D Klein bottle insulator in Ref. [52]. It may be calculated on any K^2 slice using Equations (4.2) and (4.3).

The \mathbb{Z} invariant ν_x appears to be novel; as discussed under Figure 4.12(a), it manifests as an even Chern number $C_x = 2\nu_x \in 2\mathbb{Z}$ on the full Brillouin torus, relating to the fact that the torus contains two copies of $K^2 \times S^1$. This suggests one way of calculating this invariant in practice: it may be obtained from \mathbb{T}^3 as

$$\nu_x = \frac{1}{2}C_x = \frac{1}{4\pi} \int_{\mathbb{T}_{yz}^2} \mathcal{F}, \quad (4.11)$$

where \mathbb{T}_{yz}^2 is any slice of \mathbb{T}^3 running in the yz -direction. This calculation does not generally respect the glide symmetry, since such a \mathbb{T}_{yz}^2 is not invariant outside of the

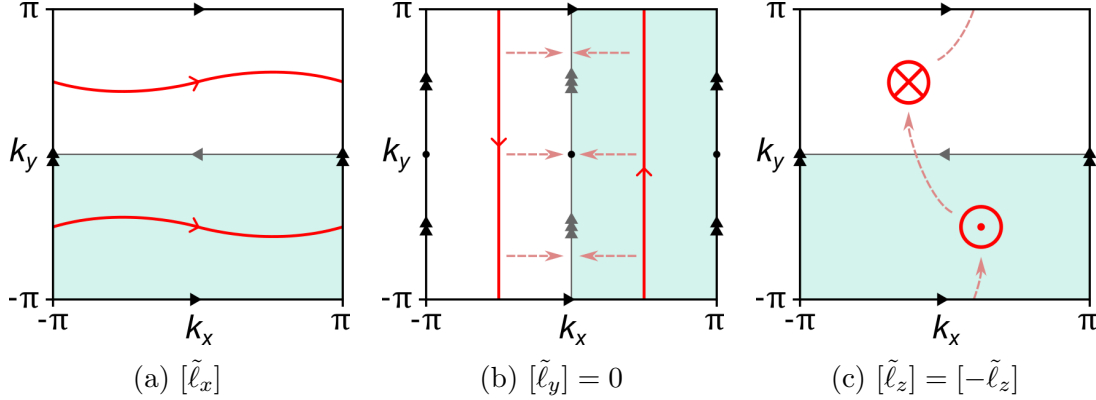


Figure 4.12: Top view of \mathbb{T}^3 . Each graphic shows one of the three basic Dirac loops $\ell_{x,y,z}$ [representing the generators of $H_1(\mathbb{T}^3)$] sitting inside a fundamental domain (shaded teal). Each loop is doubled by the action of the symmetry, into what can be considered a twisted Dirac loop $\tilde{\ell}_{x,y,z}$ [representing an invariant in $H_1(K^2 \times S^1; \mathbb{Z})$] shown in red. (a) In the case of ℓ_x , the orientation reversal cancels out the $k_x \mapsto -k_x$ parity change from the glide symmetry, and the resulting twisted Dirac string $\tilde{\ell}_x$ has a consistent orientation. It follows that the associated invariant $\nu_x \in \mathbb{Z}$ induces an even Chern number $C_x = 2\nu_x \in 2\mathbb{Z}$ on the full torus. (b) The alternative fundamental domain from Figure 4.7(c) paints a clearer picture for ℓ_y . The loop is mirrored along the glide plane $k_x = 0$ and has its orientation reversed. The resulting twisted Dirac string $\tilde{\ell}_y$ is trivial: as indicated by the dashed arrows, the two copies can be moved together while maintaining glide symmetry, and they cancel out when they meet on the glide plane. As a result, there is no invariant ν_y . (c) The Dirac loop ℓ_z running in the positive z direction (“out of the page”) in the fundamental domain is doubled to a second loop running in the negative z direction (“into the page”). In this case, the two loops cannot be brought together while respecting the symmetry, but they can be interchanged by moving them along the dashed arrows. It follows that the resulting twisted Dirac string $\tilde{\ell}_z$ is equivalent to its own inverse $-\tilde{\ell}_z$, meaning it generates a \mathbb{Z}_2 invariant ν_z .

glide planes at $k_x = 0$ and $k_x = \pm\pi$. Still, it results in the correct invariant in the insulating case: by regular Poincaré duality on the full torus, the integral over \mathbb{T}_{yz}^2 counts the number of ℓ_x -like Dirac loops, and the generator $\tilde{\ell}_x$ features precisely two such loops on the torus.⁹ We will return to the case with Weyl points when we study the full group of semimetal invariants.

⁹A Dirac loop may in principle also contain y and z components, but these do not affect this integral. From a homology perspective, such loops may be decomposed into their basic $\ell_{x,y,z}$ components because the first homology group is Abelian.

Mod 2 charge cancellation

A second feature that stands out is the appearance of a \mathbb{Z}_2 group on the far right side of the exact sequence in Equation (4.9). It is worth mentioning that this is a general feature of ordinary cohomology on non-orientable manifolds: the rightmost group is the top cohomology group of the Brillouin zone, and any non-orientable n -manifold M has $H^n(M) \cong \mathbb{Z}_2$.

Recall from Section 3.2.3 that the map Σ in Equation (4.10) can be interpreted as a sum over all Weyl point charges on \mathbb{T}^3 . The Nielsen–Ninomiya charge cancellation theorem on the torus then arises from the fact that $\Sigma \circ \beta = 0$; that is, a semimetal structure $a \in \mathbb{Z}^3 \oplus \mathbb{Z}^{k-1}$ must always feature a charge configuration $\beta(a) \in \mathbb{Z}^k$ such that the charges sum to $\Sigma(\beta(a)) = 0 \in \mathbb{Z}$.

The situation is somewhat more subtle on $K^2 \times S^1$: the \mathbb{Z}^k group $H^2\left(\bigcup_{i=1}^k S_{w_i}^2\right)$ and its dual $H_0(W; \widetilde{\mathbb{Z}})$ no longer have a direct interpretation in terms of Weyl point charges, since both the absolute and relative chiralities of these points are ill defined here—as seen in Figure 4.7. That is, the spheres S_{w_i} no longer have a canonical orientation descending from the ambient manifold. Instead, $H^2\left(\bigcup_{i=1}^k S_{w_i}^2\right)$ must be interpreted as the group of charges χ_i *given a choice of orientation* at each Weyl point w_i . This choice of orientation is exactly what is induced by choosing a specific fundamental domain: the changes of (absolute and relative) chirality in Figure 4.7 correspond to a change of basis of this \mathbb{Z}^k . Nevertheless, the map Σ can still be interpreted as a sum over these charges, precisely because it maps into \mathbb{Z}_2 : to be exact, the map

$$\Sigma : \mathbb{Z}^k \rightarrow \mathbb{Z}_2, \quad (\chi_1, \dots, \chi_k) \mapsto \sum_{i=1}^k \chi_i \mod 2 \quad (4.12)$$

is invariant under change of orientation at each w_i because

$$\chi_i \equiv -\chi_i \mod 2.$$

It follows that the tail end of the sequence (4.9) can be interpreted unambiguously in terms of \mathbb{Z}_2 charge cancellation: regardless of the parametrisation of the fundamental domain, the charges belonging to a semimetal (i.e. mapped into \mathbb{Z}^k by β) must sum to $0 \in \mathbb{Z}_2$. In other words, the total charge must be even on any fundamental domain. This is the same charge cancellation condition presented in Equation (4.5).

Importantly, the exactness of Equation (4.9) also implies the converse statement by $\text{im}(\beta) = \ker(\Sigma)$: for a given set of Weyl points $W \subset K^2 \times S^1$, any configuration of charges with an even total [i.e. an element of $\ker(\Sigma)$] must be realised in some set of semimetal invariants [i.e. be an element of $\text{im}(\beta)$]. In the homology picture, this means there must exist configurations of twisted Dirac strings in $H_1(M, W; \widetilde{\mathbb{Z}})$ realising any given set of charges adding to $0 \in \mathbb{Z}_2$.

Semimetal invariants

Finally, central to the sequence in Equation (4.9) is the group of semimetal invariants,

$$H^2(K^2 \times S^1 \setminus W) \cong H_1(K^2 \times S^1, W; \widetilde{\mathbb{Z}}) \cong \mathbb{Z} \oplus \mathbb{Z}_2 \oplus \mathbb{Z}^k. \quad (4.13)$$

Much like the $\mathbb{Z}^3 \oplus \mathbb{Z}^{k-1}$ in the case of \mathbb{T}^3 , this group does not admit a canonical basis of invariants. Rather, the exactness of Equation (4.9) around this group provides information about the structure of the different semimetallic phases. The argument is similar to that at the end of Section 3.2.3: given a charge configuration c in the image of the map β (i.e. any c with an even total charge), the pre-image must obey

$$\beta^{-1}(c) \cong \beta^{-1}(0) =: \ker(\beta),$$

since β is a homomorphism. By exactness, we have $\ker(\beta) \cong \text{im}(\alpha) \cong \mathbb{Z} \oplus \mathbb{Z}_2$. That is, for each $c \in \text{im}(\beta)$ there are $\mathbb{Z} \oplus \mathbb{Z}_2$ worth of semimetal invariants (or equivalently, twisted Dirac string configurations) in its pre-image, differing from each other by the bulk invariants $\nu_x \in \mathbb{Z}$ and $\nu_z \in \mathbb{Z}_2$.

There is a subtle difference from the argument on the torus: on \mathbb{T}^3 , \mathbb{Z} charge cancellation ensures that the valid charge configurations exist in

$$\text{im}(\beta) = \ker(\Sigma) = H^2\left(\bigcup_{i=1}^k S_{w_i}^2\right) / H^3(\mathbb{T}^3) \cong \mathbb{Z}^k / \mathbb{Z} \cong \mathbb{Z}^{k-1},$$

explaining the \mathbb{Z}^{k-1} summand in the semimetal group. This \mathbb{Z}^{k-1} cannot be given a basis in terms of the k different Weyl point charges on the semimetal, and it must be interpreted more abstractly as the set of valid charge configurations. On $K^2 \times S^1$, the \mathbb{Z}_2 charge cancellation implies that

$$\text{im}(\beta) = \ker(\Sigma) \cong \mathbb{Z}^k / \mathbb{Z}_2 \cong \mathbb{Z}^k,$$

and this is the \mathbb{Z}^k which appears in the semimetal group in Equation (4.13). Just as on the torus, we should be careful not to interpret this \mathbb{Z}^k directly in terms of the charges of the k Weyl points. Even though it contains k factors of \mathbb{Z} , not all possible combinations of charges are contained in this subgroup: after all, charge configurations with an odd total are not in the kernel of Σ . Instead, it should be considered an index 2 subgroup of the charge configurations, containing only those with an even total.

Physically, the \mathbb{Z}^k summand in the semimetal group implies that a system with a single Weyl point ($k = 1$) on $K^2 \times S^1$ may already feature semimetal topology. The single Weyl point must have even charge by \mathbb{Z}_2 charge cancellation; an example of such a system is featured in the supplement to Ref. [7] and reproduced in Figure 4.13.

Finally, we have seen in Section 3.2.2 that the Chern number on a 2D slice of \mathbb{T}^3 changes by $q \in \mathbb{Z}$ as the slice is passed over a Weyl point of charge q . We might expect this to be problematic in the non-orientable case, given that the Brillouin zone is periodic and the total charge need not add up to zero. This is resolved in two different ways for the two invariants ν_x and ν_z . The latter is saved by being a \mathbb{Z}_2 invariant, restoring the periodicity over an even total charge—as was also observed in Ref. [7].

The \mathbb{Z} invariant ν_x requires us to define the integration more carefully: as noted before, the integration in Equation (4.11) does not respect the symmetry, and it may not yield the right invariant when Weyl points are introduced. This is illustrated

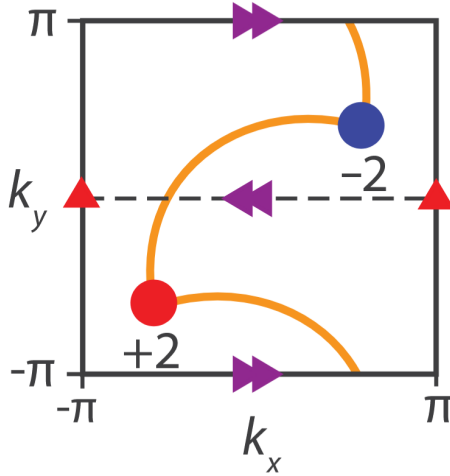


Figure 4.13: Figure from the supplement to Ref. [7]. Originally intended as a surface Brillouin zone with Fermi arcs, it can be interpreted equally well as a top view of a 3D system with two Dirac strings. Both Dirac strings are oriented towards the positively charged point.

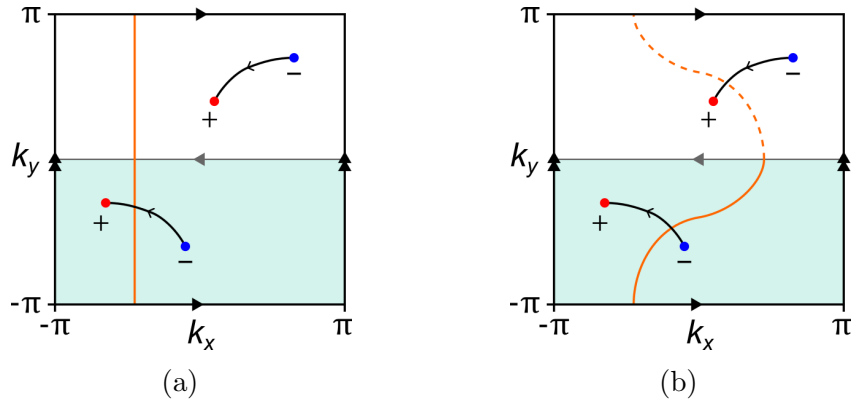


Figure 4.14: (a) In the presence of Weyl points, a given \mathbb{T}_{yz}^2 (orange) may only intersect a single Dirac string, leading to a non-integer value of $1/2$ from Equation (4.11). (b) Integration over an invariant surface always yields a well defined ν_x outside of Weyl points, since it intersects the twisted Dirac strings in a consistent manner. The dashed half of the surface is redundant, since both halves yield the same integral. The pictured setup yields $\nu_x = 1$.

in Figure 4.14(a). Instead, it becomes necessary to integrate over a symmetry-invariant surface S which is continuously deformable to a \mathbb{T}_{yz}^2 , such as that shown in Figure 4.14(b). This is similar in spirit to the \mathcal{T} -invariant surfaces used to calculate invariants in the time-reversal symmetric case [29]. In principle, only the half of the surface $S_{1/2}$ which intersects the fundamental domain at $k_y \leq 0$ needs to be integrated over; this half surface can be considered a compact surface subspace of $K^2 \times S^1$. The calculation then takes the form

$$\nu_x = \frac{1}{2\pi} \int_{S_{1/2}} \mathcal{F}. \quad (4.14)$$

The question of periodicity is now resolved by the fact that the surface S cannot be moved across the entire Brillouin zone without breaking the symmetry: any such surface can be deformed equivariantly into exactly one of the glide planes at $k_x = 0$ and $k_x = \pm\pi$, but one cannot be deformed into the other. For example, if we start with S at the $k_x = 0$ plane and perturb a small section of S continuously in the positive x direction, then another section must be moved in the negative x direction at the same time to maintain glide symmetry. By continuity, it follows that S must still intersect $k_x = 0$ somewhere.¹⁰ As such, there is no deformation that can completely remove S from the $k_x = 0$ plane, and in particular it cannot be taken fully to the glide plane at $k_x = \pm\pi$. An analogous argument holds the other way around.¹¹

As a final remark, we note that the only \mathbb{Z}_2 factor in the semimetal group in Equation (4.13) stems directly from the underlying insulating topology; any Weyl points that are added only introduce additional \mathbb{Z} factors. As such, it is the opinion of the author that no intrinsic \mathbb{Z}_2 charge should be assigned to Weyl points, as is done in Ref. [7].¹² Instead, the \mathbb{Z}_2 invariant on gapped K^2 -like slices should be taken to be directly influenced by the \mathbb{Z} charge on Weyl points. To be precise, if such a slice with invariant ν_z is moved over a Weyl point of charge C in the k_z direction, the new \mathbb{Z}_2 invariant is

$$\nu'_z = \nu_z + C \mod 2,$$

requiring no \mathbb{Z}_2 charge on the Weyl point. This is also the position taken with respect to time-reversal invariant Weyl semimetals in Ref. [29].

4.3 Conclusions and outlook

[Should outlook be a stand-alone chapter?]

Outlook points:

- The K^2 surface topology is probably also easily captured using twisted homology/ordinary 1st cohomology. The other two surfaces are more complicated: in the front (xz) surface, the chirality change is induced by mirroring across $k_x = 0$ (probably can be captured using equivariant cohomology on the surface), while in the yz surface it is induced by a change of projection direction (cannot be captured using equivariant homology, the effective surface BZ is a torus).

¹⁰The argument can be formalised using the mean-value theorem if we take the momenta to live in \mathbb{R}^3 rather than identifying equivalent momenta into a torus.

¹¹By the same logic, we can generally infer which of the two glide planes S deforms to by studying these intersections: for example, the surface in Figure 4.14(b) does not intersect the plane at $k_x = \pm\pi$, and so it must deform to $k_x = 0$. In general, we can count the number of times S intersects with $k_x = 0$ in the range $-\pi < k_y \leq 0$ (at any k_z); an odd number of intersections [such as the single crossing in the fundamental domain in Figure 4.14(b)] indicates that the surface deforms to $k_x = 0$.

¹²Explicit calculations are provided for this \mathbb{Z}_2 charge in Ref. [7], but these rely on integration over K^2 -like tubes spanning the fundamental domain in the k_y direction. As a result, these invariants are an expression of the global topology of $K^2 \times S^1 \setminus W$, not the local topology around a Weyl point.

- This description may be easily extendable to a 2D type A III Klein bottle WSM with chiral symmetry; in this case, 1st cohomology invariants (winding numbers) are dual to twisted 1st homology invariants (Fermi arcs/loops).
- More elementary systems such as 3D type A with inversion symmetry also exhibit non-orientable EBZs, but in this case the description is complicated by the existence of fixed points (the TRIM).
- Applicability of this description is probably limited under addition of non-trivial additional bands, e.g. 4-band models incorporating spin and orbital degrees of freedom. The full scope of applicability is somewhat of an open question at this point. (E.g., how well are 2D chiral WSMs described by this homology picture?)
- Experimental verification in acoustic crystals may be relatively straightforward.
- Anti-unitary glide symmetry \implies twisted cohomology on $K^2 \times S^1$?

Notes

Concepts explored in early personal notes:

- Calculations of (co)homology and semimetal MV sequence for manifolds in ≥ 2 dimensions:
 - All compact surfaces without boundary, i.e. the surfaces M_g and N_g
 - All spaces of the form $M = K^2 \times \mathbb{T}^{d-2}$
- The map $\Sigma : H^{d-1}(\bigsqcup_k S^{d-1}) \rightarrow H^d(M)$ in the semimetal MV has a clear interpretation in terms of total charge in the (orientable) $d = 3$ case. This would provide a clear picture of the total charge cancellation in the orientable case ($H^d(M) = \mathbb{Z}$ in general) vs. the mod 2 charge cancellation in the non-orientable case ($H^d(M) = \mathbb{Z}_2$ in general).
- However, Σ and the other maps in the MV sequence are difficult to interpret in the $\chi \neq 0$ case (maybe even generally for odd dimensions). Taking the oriented case as an example, the MV sequence ends as

$$H^{d-1}(M \setminus \Delta) \rightarrow H^{d-1}\left(\bigsqcup_k S^{d-1}\right) \cong \mathbb{Z}^k \xrightarrow{\Sigma} H^d(M) \cong \mathbb{Z}$$

so that the “charge configuration” in \mathbb{Z}^k must map to 0 by Σ in order to descend from the semimetal, regardless of whether $\chi = 0$.

- This may imply that the Bloch vector field carries more topological information about the total charge than the MV sequence (which makes sense since it generates *all* homology groups of the valence bundle, and all Betti numbers factor into χ). As a concrete example, consider $M = S^2$ with a single puncture

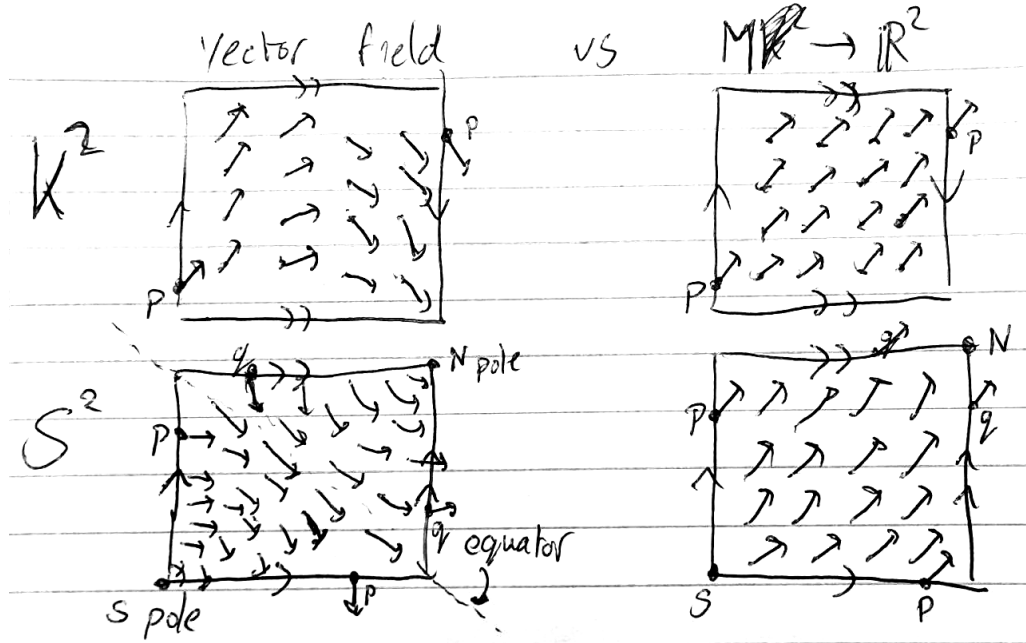
of charge +2. The punctured sphere is topologically a disc, so that the valence bundle must be trivial, while the Bloch vector field is topologically non-trivial in the sense that it has an index +2 singularity. In addition, all relevant $H_n(A) \oplus H_n(B)$ are zero, so that the semimetal MV reduces to the statement that $H_2(S^2) \cong H_1(S^1)$.

- It may even be the case that the valence bundle cannot be generated from the Bloch vector field in the $d = 2$ case; it's probably worth studying the $d \in \{3, 4, 5\}$ cases (pullback of some universal bundle) to learn more about this. The $d = 3$ case should be especially helpful in understanding how the valence bundle arises from the vector field.
- A complicating factor in the non-orientable case is that the homology groups are different from the cohomology groups, since the torsion moves up one dimension. This makes the homological semimetal MV different from the cohomological one (it's a short exact sequence in $d \geq 3!$), and this leads to additional challenges in interpretation.
- The map $H : \mathbb{R}^3 \rightarrow \mathfrak{su}(2)$, $\vec{h} \mapsto \vec{h} \cdot \vec{\sigma}$ is an isomorphism of Lie algebras, with the cross product as a Lie bracket on \mathbb{R}^3 . Still the vector field is discontinuous on a non-orientable manifold, while H is not. This suggests an alternative approach for constructing the valence bundle: consider h as a map $M \rightarrow \mathbb{R}^d$ instead of an element of $\mathfrak{X}(M)$, and then pull back the universal bundle along the unit map $\hat{h} : M \setminus \Delta \rightarrow S^{d-1}$. That is, we detach \vec{h} from the tangent bundle and consider it a more abstract map. An added “benefit” of this is that we lose all coordinate dependence. However, this may also be a downside in the sense that the map will not be subject to the same constraints (Poincaré–Hopf etc.) that the vector field is; for example, $S^2 \rightarrow \mathbb{R}^2$, $x \mapsto (1, 0)$ is a perfectly valid map that would violate the hairy ball theorem as a vector field (and this is a result of being unable to cover S^2 by a single chart). At this point the question may become more about which description is more physical in nature, and the non-orientable Weyl point paper[7] seems to imply there may be more to the $h : M \rightarrow \mathbb{R}^3$ story. It also seems to agree better with the intuition of an applied external potential removing all Weyl nodes – something that's impossible for $\chi \neq 0$ if charge corresponds to vector field index. It also explains how the valence bundle can be trivial on the once punctured S^2 .
- In light of the previous point, this may be an important observation: every d -manifold M with $\chi(M) = 0$ admits a nowhere-vanishing vector field (link). This may imply that the vector field description is equivalent to the map to \mathbb{R}^d in these cases, though one needs to be careful about charts. It would be good to find or write a (dis)proof for something like $\mathfrak{X}(M) \cong C^\infty(M, \mathbb{R}^d)$ (or similar for non-vanishing maps) in this case. Or more specifically:

$$[M \setminus \Delta, S^{d-1}] \xrightarrow{?} \left\{ \vec{h} \in \mathfrak{X}(M \setminus \Delta) \mid \vec{h} \text{ is non-vanishing} \right\}$$

Update: I think the real requirement for equivalence is that the base manifold M is parallelisable (i.e. has a trivial tangent bundle), since we're essentially using a trivial \mathbb{R}^d -bundle in this construction.

- Any smooth d -manifold can be given a CW complex structure with one d -cell (link). On this d -cell there is an exact correspondence between vector fields and maps to \mathbb{R}^d , since it can be embedded in \mathbb{R}^d . What distinguishes the two is how points on the boundary of the d -cell are identified with each other; this determines whether the “vectors” need to change orientation. To illustrate:



- On any orientable manifold, the Stokes' theorem argument shows that the total charge must be zero regardless of Euler characteristic:

$$\sum_{\alpha} w(S_{\alpha}) = \sum_{\alpha} \int_{S_{\alpha}} c_1(E) = \sum_{\alpha} \int_{S_{\alpha}} \frac{\text{Tr } \mathcal{F}}{2\pi} = \int_{B'} d \frac{\text{Tr } \mathcal{F}}{2\pi} = 0$$

where the last equality holds by the Bianchi identity for the trace. This means the valence bundle cannot be a pullback along a tangent vector field for $\chi \neq 0$.

On a non-orientable manifold, this argument doesn't hold since the integral over B' isn't well defined.

- Total chirality isn't well defined on a non-orientable manifold (at least in odd dimensions, not sure how to interpret even dimensions). Still there is charge cancellation in the form of Fermi arcs etc.; it may take moving to a different homology system to get the full picture, such as homology with local coefficients or equivariant homology. (See e.g. Ref. [29])
- It may be worth classifying which manifolds are candidates for physical material Brillouin zones; I have a feeling that this might be restricted to those manifolds for which the n -torus is a covering space. In this case a full classification of symmetries on the torus (and e.g. their related equivariant homologies) would be sufficient to classify all material topologies. This classification is related to space group symmetries.

Appendix A

Homology and cohomology

The concepts of homology and its dual counterpart cohomology are indispensable tools in the mathematical field of algebraic topology. While seemingly abstract to from a physics point of view, many fundamental elements of the physicist's toolbox—such as Stokes' theorem—are formulated most naturally in the context of this theory.

Here we offer a brief introduction to these concepts, aimed at the uninitiated physicist. The goal here is not to be completely rigorous, but to give a sufficiently comprehensive understanding that the applications discussed in the main text may be understood in their proper context. For a more complete picture, the interested reader is referred to standard texts in algebraic topology such as Refs. [28] and [62]. A more geometric treatment relying on differential forms is also found in Ref. [63].

The basic idea underlying homology is that information about the topology of a space M can be gained from studying non-trivial subspaces of M of various dimensions. Perhaps the simplest conceptual realisation of this idea exists in the closely related *homotopy* theory. In this theory, one defines the n th homotopy group $\pi_n(M)$ in terms of maps from the n -dimensional sphere S^n into M . For example, the first homotopy group $\pi_1(M)$ (also known as the *fundamental group*) records the topologically different ways in which loops $\gamma : S^1 \rightarrow M$ can sit inside M . If two such loops cannot be transformed continuously into each other, then they represent different elements of $\pi_1(M)$.

Despite their conceptual simplicity, homotopy groups can be rather unwieldy in practice: they are generally difficult to calculate and may have unpredictable structures. For example, even maps from S^n to a lower-dimensional S^m with $m < n$ may be non-trivial, and calculating the associated higher homotopy groups $\pi_n(S^m)$ of the spheres is an important open problem in algebraic topology.

This is where the closely related homology enters the stage. It is conceptually somewhat more involved than homotopy, and strictly speaking it contains less information. However, there is a great payoff: homology groups are generally much easier to compute and structurally simpler than their homotopy counterparts. Moreover, homology can be dualized into cohomology, which is a construction which is both mathematically and physically very natural.

Homology

The basic building blocks of homology theory are oriented subspaces of a space M .¹ Some such subspaces are illustrated for the two-dimensional torus in Figure A.1. Topological information can be gained from these subspaces by studying their

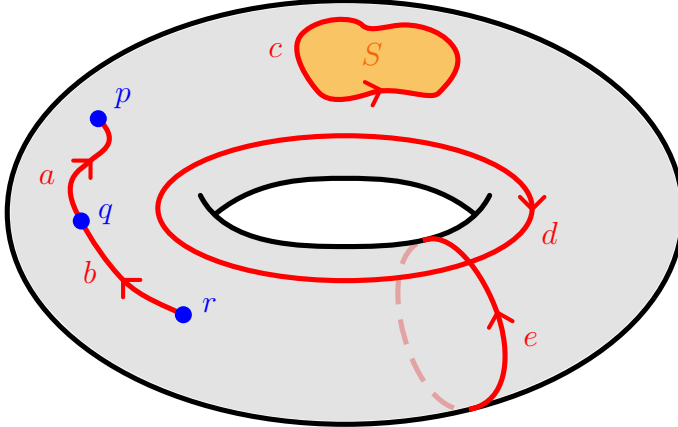


Figure A.1: The two-torus \mathbb{T}^2 . Some of the oriented subspaces that make up chains in the homology theory are highlighted: components of 0, 1, and 2-chains are coloured blue, red and orange, respectively. The orientation of the 0D and 2D subspaces can be canonically induced from an orientation on the torus in this case.

(oriented) boundaries. The goal of homology is to find subspaces such as d and e in Figure A.1, which do not have a boundary, but cannot themselves be written as the boundary of another subset either—unlike c , for instance, which is the boundary of S . Spaces like d and e detect topological features of the space, such as the hole in the centre of the torus.

To properly define oriented boundaries, we must work in the context of so-called *n-chains*, which are linear combinations of n -dimensional subspaces of M . For example, $a + b$ is a 1-chain on the torus in Figure A.1, as is $3a - 2c$. Using *n*-chains makes boundaries well-behaved under addition. For example, we may define the boundary of a as the 0-chain $\partial a = p - q$, and similarly $\partial b = q - r$; adding these up, we obtain

$$\partial a + \partial b = (p - q) + (q - r) = p - r,$$

which is precisely the boundary of the 1-chain $a + b$.

Formally, an *n*-chain takes the form

$$\sum_i c_i X_i,$$

where $X_i \subset M$ are oriented n -dimensional subsets of M . The coefficients c_i are usually taken to be integers in \mathbb{Z} , but they may also be e.g. real numbers, rationals

¹There are several different ways of formally defining these oriented subspaces, such as mapping simplices (the n -dimensional analog of triangles) into M or defining a so-called *cell structure* on M . Importantly, these different constructions usually give rise to the same homology groups; because of this, we will be agnostic to the details and focus on the conceptual basis instead.

or elements of \mathbb{Z}_2 ; to be precise, they must be elements of any fixed Abelian group G , which is called the *coefficient group*. A powerful result called the universal coefficient theorem tells us that taking coefficients in the integers $G = \mathbb{Z}$ always results in the richest possible homology theory; this is why the coefficients are usually assumed to be elements of \mathbb{Z} unless explicitly stated otherwise.

The n -chains on M naturally form a group under addition in the coefficient group G , which we notate $C_n(M; G)$ —or simply $C_n(M)$ when $G = \mathbb{Z}$. The inverses in this group act to invert the orientation of a chain: for example, the chain $-c$ on our torus looks like c with the arrow pointing in the opposite direction.

The boundary of an n -chain is always an $(n - 1)$ -chain. This is even true for $n = 0$; points have no boundary, so their boundary is the empty “ (-1) -chain” in $C_{-1}(M; G) = 0$. This means taking the boundary defines² a map ∂_n from $C_n(M; G)$ to $C_{n-1}(M; G)$ for every integer n . These maps are group homomorphisms—that is, for integer or real coefficients, they are linear: for instance, we have already seen that $\partial(a + b) = \partial a + \partial b$ on our torus.

The boundary maps ∂_n can be used to arrange the chain groups in a so-called *chain complex*:

$$0 \xleftarrow{\partial_0} C_0(M; G) \xleftarrow{\partial_1} C_1(M; G) \xleftarrow{\partial_2} C_2(M; G) \xleftarrow{\partial_3} \dots .$$

These chain complexes are usually finite: for example, the 2-torus in Figure A.1 has no 3-dimensional subspaces, so its chain complex (with integer coefficients) reads

$$0 \xleftarrow{\partial_0} C_0(\mathbb{T}^2) \xleftarrow{\partial_1} C_1(\mathbb{T}^2) \xleftarrow{\partial_2} C_2(\mathbb{T}^2) \xleftarrow{\partial_3} 0.$$

In practice, the subscript on the maps ∂_n is often dropped when talking about specific subspaces.

A very important property of the chain complex is that composing two boundary maps always yields zero; this is often abbreviated as $\partial^2 = 0$. In other words, boundaries have no boundaries. An example of this can be seen in Figure A.1: the 1-chain c is the boundary of the 2-chain S , but it does not have a boundary itself. In homology terms, chains like c which have no boundaries are called *cycles*. The set of n -cycles is denoted Z_n and it forms a subgroup of the n -chain group. It is defined in terms of the kernel of ∂_n , i.e. the n -chains that map to the empty chain 0:

$$Z_n(M; G) := \ker(\partial_n) \subset C_n(M; G).$$

The property $\partial^2 = 0$ implies that all boundaries are cycles, but crucially, it does not imply the opposite: there may be cycles which are not boundaries. In Figure A.1, d and e are such 1-cycles: we cannot find a 2-chain of which d is the boundary, for instance. This implies that the set of n -chains which are boundaries is a subgroup of the group of n -cycles Z_n . The former group is called the group of n -boundaries and denoted B_n . It is defined as the image of ∂_{n+1} :

$$B_n(M; G) := \text{im}(\partial_{n+1}) \subset Z_n(M; G) \subset C_n(M; G).$$

²The precise definition of the boundary map depends on the way subspaces are defined, but the properties we discuss here are universal.

We can now finally define the homology on M . The n th homology group H_n consists of all n -cycles modulo n -boundaries:

$$H_n(M; G) := \frac{Z_n(M; G)}{B_n(M; G)} = \ker(\partial_n)/\text{im}(\partial_{n+1}).$$

Again, the coefficient group G is often dropped from the notation under integer coefficients $G = \mathbb{Z}$. The elements of H_n are called *homology classes*, and they are equivalence classes of n -cycles. Two n -cycles γ_1 and γ_2 are called *homologous* if they differ only by a boundary, i.e. if $\gamma_1 = \gamma_2 + \partial\Gamma$ for some $n+1$ chain Γ . In this case they represent the same homology class, and we write $[\gamma_1] = [\gamma_2] \in H_n(M; G)$. For example, the 1-cycle c in Figure A.1 is the boundary of the 2-chain S , and so it is homologous to the empty cycle: $c = 0 + \partial S$, meaning $[c] = 0 \in H_1(\mathbb{T}^2)$. Similarly, any n -boundary represents the trivial class in H_n in general. Intuitively, this is because a boundary can always be continuously retracted to a point (for example, c can be retracted by shrinking S), where it vanishes and becomes the empty cycle.

Another important example of homologous cycles is illustrated in Figure A.2. In

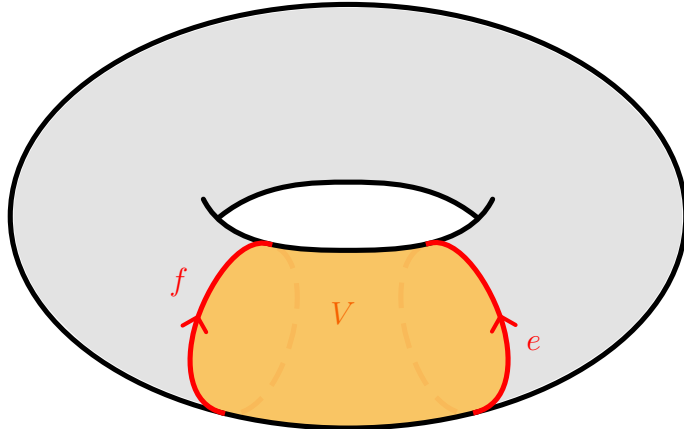


Figure A.2: The 2-torus \mathbb{T}^2 , featuring the same 1-cycle e as before, and also a 1-cycle f which is obtained by moving e along the torus. The boundary of the 2-chain V indicated in orange is precisely the difference of these cycles: $\partial V = e - f$. Since e and f differ by a boundary, they are homologous, i.e. $[e] = [f] \in H_1(\mathbb{T}^2)$.

this case, we see that non-trivial cycles may also represent the same homology class if they can be deformed into each other continuously.

These examples demonstrate an important general property: the homology group classifies cycles that differ from each other topologically, i.e. cannot be deformed into one another. As a result, the homology groups H_n have a much simpler structure than the underlying chain groups. For example, the first homology group of the 2-torus $H_1(\mathbb{T}^2)$ consists precisely of elements of the form

$$m_d[d] + m_e[e], \quad m_d, m_e \in G = \mathbb{Z},$$

where d and e are as in Figure A.1. It follows that this group looks like two copies of \mathbb{Z} :

$$H_1(\mathbb{T}^2) \cong \mathbb{Z}^2.$$

The 0th homology group can be obtained by similar logic: all single points on \mathbb{T}^2 can be continuously moved to a single point p , so that elements of $H_0(\mathbb{T}^2)$ are of the form

$$m_p[p], \quad m_p \in \mathbb{Z},$$

and consequently

$$H_0(\mathbb{T}^2) \cong \mathbb{Z}.$$

For similar reasons, if M consists of k connected components, then $H_0(M) = \mathbb{Z}^k$ in general.

Finally, the only two-dimensional subspace of \mathbb{T}^2 that represents a non-trivial homology class turns out to be the whole torus itself; as a result, H_2 also has a single generator:

$$H_2(\mathbb{T}^2) \cong \mathbb{Z}.$$

Cohomology

Bibliography

- [1] Anton Akhmerov et al. *Online course on topology in condensed matter*. URL: <https://topocondmat.org/> (visited on 10/07/2024).
- [2] János K. Asbóth, László Oroszlány, and András Pályi. *A Short Course on Topological Insulators*. Springer International Publishing, 2016. ISBN: 9783319256078. DOI: 10.1007/978-3-319-25607-8. URL: <http://dx.doi.org/10.1007/978-3-319-25607-8>.
- [3] B. Andrei Bernevig and Taylor L. Hughes. *Topological insulators and topological superconductors*. Princeton University Press, 2013. ISBN: 978-0-691-15175-5.
- [4] Masatoshi Sato and Yoichi Ando. “Topological superconductors: a review”. In: *Reports on Progress in Physics* 80.7 (May 2017), p. 076501. ISSN: 1361-6633. DOI: 10.1088/1361-6633/aa6ac7. URL: <http://dx.doi.org/10.1088/1361-6633/aa6ac7>.
- [5] P. Gehring et al. “A Natural Topological Insulator”. In: *Nano Letters* 13.3 (Mar. 2013), pp. 1179–1184. ISSN: 1530-6992. DOI: 10.1021/nl304583m. URL: <http://dx.doi.org/10.1021/nl304583m>.
- [6] Felix Bloch. “Über die Quantenmechanik der Elektronen in kristallgittern”. In: *Zeitschrift für Physik* 52.7–8 (July 1929), pp. 555–600. DOI: 10.1007/bf01339455.
- [7] André Grossi Fonseca et al. “Weyl Points on Nonorientable Manifolds”. In: *Phys. Rev. Lett.* 132 (26 June 2024), p. 266601. DOI: 10.1103/PhysRevLett.132.266601. URL: <https://link.aps.org/doi/10.1103/PhysRevLett.132.266601>.
- [8] W. P. Su, J. R. Schrieffer, and A. J. Heeger. “Solitons in Polyacetylene”. In: *Phys. Rev. Lett.* 42 (25 June 1979), pp. 1698–1701. DOI: 10.1103/PhysRevLett.42.1698. URL: <https://link.aps.org/doi/10.1103/PhysRevLett.42.1698>.
- [9] W. P. Su, J. R. Schrieffer, and A. J. Heeger. “Soliton excitations in polyacetylene”. In: *Phys. Rev. B* 22 (4 Aug. 1980), pp. 2099–2111. DOI: 10.1103/PhysRevB.22.2099. URL: <https://link.aps.org/doi/10.1103/PhysRevB.22.2099>.
- [10] Michael Freedman et al. “A class of P,T-invariant topological phases of interacting electrons”. In: *Annals of Physics* 310.2 (2004), pp. 428–492. ISSN: 0003-4916. DOI: <https://doi.org/10.1016/j.aop.2004.01.006>. URL: <https://www.sciencedirect.com/science/article/pii/S0003491604000260>.

- [11] Eric J Meier, Fangzhao Alex An, and Bryce Gadway. “Observation of the topological soliton state in the Su–Schrieffer–Heeger model”. en. In: *Nat. Commun.* 7.1 (Dec. 2016), p. 13986.
- [12] Marcos Atala et al. “Direct measurement of the Zak phase in topological Bloch bands”. In: *Nature Physics* 9.12 (Nov. 2013), pp. 795–800. ISSN: 1745-2481. DOI: 10.1038/nphys2790. URL: <http://dx.doi.org/10.1038/nphys2790>.
- [13] A.A. Burkov. “Weyl Metals”. In: *Annual Review of Condensed Matter Physics* 9.1 (Mar. 2018), pp. 359–378. ISSN: 1947-5462. DOI: 10.1146/annurev-conmatphys-033117-054129. URL: <http://dx.doi.org/10.1146/annurev-conmatphys-033117-054129>.
- [14] Alexey A Soluyanov et al. “Type-II Weyl semimetals”. In: *Nature* 527.7579 (Nov. 2015), pp. 495–498.
- [15] H.B. Nielsen and M. Ninomiya. “Absence of neutrinos on a lattice: (I). Proof by homotopy theory”. In: *Nuclear Physics B* 185.1 (1981), pp. 20–40. ISSN: 0550-3213. DOI: [https://doi.org/10.1016/0550-3213\(81\)90361-8](https://doi.org/10.1016/0550-3213(81)90361-8). URL: <https://www.sciencedirect.com/science/article/pii/0550321381903618>.
- [16] H.B. Nielsen and M. Ninomiya. “Absence of neutrinos on a lattice: (II). Intuitive topological proof”. In: *Nuclear Physics B* 193.1 (1981), pp. 173–194. ISSN: 0550-3213. DOI: [https://doi.org/10.1016/0550-3213\(81\)90524-1](https://doi.org/10.1016/0550-3213(81)90524-1). URL: <https://www.sciencedirect.com/science/article/pii/0550321381905241>.
- [17] Pavan Hosur and Xiaoliang Qi. “Recent developments in transport phenomena in Weyl semimetals”. In: *Comptes Rendus Physique* 14.9 (2013). Topological insulators / Isolants topologiques, pp. 857–870. ISSN: 1631-0705. DOI: <https://doi.org/10.1016/j.crhy.2013.10.010>. URL: <https://www.sciencedirect.com/science/article/pii/S1631070513001710>.
- [18] Hongming Weng et al. “Weyl Semimetal Phase in Noncentrosymmetric Transition-Metal Monophosphides”. In: *Phys. Rev. X* 5 (1 Mar. 2015), p. 011029. DOI: 10.1103/PhysRevX.5.011029. URL: <https://link.aps.org/doi/10.1103/PhysRevX.5.011029>.
- [19] Shin-Ming Huang et al. “A Weyl Fermion semimetal with surface Fermi arcs in the transition metal monopnictide TaAs class”. In: *Nature Communications* 6.1 (June 2015), p. 7373.
- [20] B Q Lv et al. “Observation of Weyl nodes in TaAs”. In: *Nature Physics* 11.9 (Sept. 2015), pp. 724–727.
- [21] Su-Yang Xu et al. “Discovery of a Weyl fermion state with Fermi arcs in niobium arsenide”. In: *Nature Physics* 11.9 (Sept. 2015), pp. 748–754.
- [22] Ilya Belopolski et al. “Signatures of a time-reversal symmetric Weyl semimetal with only four Weyl points”. In: *Nature Communications* 8.1 (Oct. 2017), p. 942.
- [23] Varghese Mathai and Guo Chuan Thiang. “Differential Topology of Semimetals”. In: *Communications in Mathematical Physics* 355.2 (July 2017), pp. 561–602. ISSN: 1432-0916. DOI: 10.1007/s00220-017-2965-z. URL: <http://dx.doi.org/10.1007/s00220-017-2965-z>.

- [24] Varghese Mathai and Guo Chuan Thiang. “Global topology of Weyl semimetals and Fermi arcs”. In: *Journal of Physics A: Mathematical and Theoretical* 50.11 (Feb. 2017), 11LT01. ISSN: 1751-8121. DOI: 10.1088/1751-8121/aa59b2. URL: <http://dx.doi.org/10.1088/1751-8121/aa59b2>.
- [25] David Vanderbilt. *Berry Phases in Electronic Structure Theory: Electric Polarization, Orbital Magnetization and Topological Insulators*. Cambridge University Press, 2018, pp. 215–218. DOI: <https://doi.org/10.1017/9781316662205>.
- [26] Gui-Geng Liu et al. “Topological Chern vectors in three-dimensional photonic crystals”. In: *Nature* 609 (2022), pp. 925–930. DOI: 10.1038/s41586-022-05077-2.
- [27] Chiara Devescovi et al. “Cubic 3D Chern photonic insulators with orientable large Chern vectors”. In: *Nature Communications* 12.1 (Dec. 2021), p. 7330.
- [28] Allen Hatcher. *Algebraic Topology*. Cambridge: Cambridge Univ. Press, 2002. URL: <https://pi.math.cornell.edu/~hatcher/AT/ATpage.html> (visited on 10/07/2024).
- [29] Guo Chuan Thiang, Koji Sato, and Kiyonori Gomi. “Fu–Kane–Mele monopoles in semimetals”. In: *Nuclear Physics B* 923 (Oct. 2017), pp. 107–125. ISSN: 0550-3213. DOI: 10.1016/j.nuclphysb.2017.07.018. URL: <http://dx.doi.org/10.1016/j.nuclphysb.2017.07.018>.
- [30] Giuseppe De Nittis and Kiyonori Gomi. “Classification of “Quaternionic“ Bloch–Bundles”. In: *Communications in Mathematical Physics* 339.1 (Oct. 2015), pp. 1–55.
- [31] Giuseppe De Nittis and Kiyonori Gomi. “The cohomological nature of the Fu–Kane–Mele invariant”. In: *Journal of Geometry and Physics* 124 (2018), pp. 124–164. ISSN: 0393-0440. DOI: <https://doi.org/10.1016/j.geomphys.2017.10.007>. URL: <https://www.sciencedirect.com/science/article/pii/S0393044017302607>.
- [32] Zhijun Wang et al. “Hourglass fermions”. In: *Nature* 532.7598 (Apr. 2016), pp. 189–194.
- [33] Yige Chen, Heung-Sik Kim, and Hae-Young Kee. “Topological crystalline semimetals in nonsymmorphic lattices”. In: *Phys. Rev. B* 93 (15 Apr. 2016), p. 155140. DOI: 10.1103/PhysRevB.93.155140. URL: <https://link.aps.org/doi/10.1103/PhysRevB.93.155140>.
- [34] Heejae Kim and Shuichi Murakami. “Emergent spinless Weyl semimetals between the topological crystalline insulator and normal insulator phases with glide symmetry”. In: *Phys. Rev. B* 93 (19 May 2016), p. 195138. DOI: 10.1103/PhysRevB.93.195138. URL: <https://link.aps.org/doi/10.1103/PhysRevB.93.195138>.
- [35] Ken Shiozaki, Masatoshi Sato, and Kiyonori Gomi. “Topology of nonsymmorphic crystalline insulators and superconductors”. In: *Phys. Rev. B* 93 (19 May 2016), p. 195413. DOI: 10.1103/PhysRevB.93.195413. URL: <https://link.aps.org/doi/10.1103/PhysRevB.93.195413>.

- [36] Tomáš Bzdušek et al. “Nodal-chain metals”. In: *Nature* 538.7623 (Oct. 2016), pp. 75–78.
- [37] Benjamin J. Wieder and C. L. Kane. “Spin-orbit semimetals in the layer groups”. In: *Phys. Rev. B* 94 (15 Oct. 2016), p. 155108. DOI: 10.1103/PhysRevB.94.155108. URL: <https://link.aps.org/doi/10.1103/PhysRevB.94.155108>.
- [38] Y. X. Zhao and Andreas P. Schnyder. “Nonsymmorphic symmetry-required band crossings in topological semimetals”. In: *Phys. Rev. B* 94 (19 Nov. 2016), p. 195109. DOI: 10.1103/PhysRevB.94.195109. URL: <https://link.aps.org/doi/10.1103/PhysRevB.94.195109>.
- [39] Bohm-Jung Yang et al. “Topological semimetals protected by off-centered symmetries in nonsymmorphic crystals”. In: *Phys. Rev. B* 95 (7 Feb. 2017), p. 075135. DOI: 10.1103/PhysRevB.95.075135. URL: <https://link.aps.org/doi/10.1103/PhysRevB.95.075135>.
- [40] Luyang Wang, Shao-Kai Jian, and Hong Yao. “Hourglass semimetals with nonsymmorphic symmetries in three dimensions”. In: *Phys. Rev. B* 96 (7 Aug. 2017), p. 075110. DOI: 10.1103/PhysRevB.96.075110. URL: <https://link.aps.org/doi/10.1103/PhysRevB.96.075110>.
- [41] Shan-Shan Wang et al. “Hourglass Dirac chain metal in rhenium dioxide”. In: *Nature Communications* 8.1 (Nov. 2017), p. 1844.
- [42] Benjamin J. Wieder et al. “Wallpaper fermions and the nonsymmorphic Dirac insulator”. In: *Science* 361.6399 (July 2018), pp. 246–251. ISSN: 1095-9203. DOI: 10.1126/science.aan2802. URL: <http://dx.doi.org/10.1126/science.aan2802>.
- [43] Xiaoliang Xiao et al. “Ideal hourglass-type charge-three Weyl fermions in spinless systems”. In: *Phys. Rev. B* 109 (7 Feb. 2024), p. 075160. DOI: 10.1103/PhysRevB.109.075160. URL: <https://link.aps.org/doi/10.1103/PhysRevB.109.075160>.
- [44] Rui-Xing Zhang and Chao-Xing Liu. *Nonsymmorphic Symmetry Protected Dirac, Möbius, and Hourglass Fermions in Topological Materials*. 2022. arXiv: 2207.00020 [cond-mat.mes-hall]. URL: <https://arxiv.org/abs/2207.00020>.
- [45] Chen Zhang et al. “General Theory of Momentum-Space Nonsymmorphic Symmetry”. In: *Phys. Rev. Lett.* 130 (25 June 2023), p. 256601. DOI: 10.1103/PhysRevLett.130.256601. URL: <https://link.aps.org/doi/10.1103/PhysRevLett.130.256601>.
- [46] Z Y Chen et al. “Classification of time-reversal-invariant crystals with gauge structures”. In: *Nature Communications* 14.1 (Feb. 2023), p. 743. DOI: 10.1038/s41467-023-36447-7.
- [47] Y. X. Zhao, Yue-Xin Huang, and Shengyuan A. Yang. “ \mathbb{Z}_2 -projective translational symmetry protected topological phases”. In: *Phys. Rev. B* 102 (16 Oct. 2020), p. 161117. DOI: 10.1103/PhysRevB.102.161117. URL: <https://link.aps.org/doi/10.1103/PhysRevB.102.161117>.

- [48] Y. X. Zhao et al. “Switching Spinless and Spinful Topological Phases with Projective PT Symmetry”. In: *Phys. Rev. Lett.* 126 (19 May 2021), p. 196402. DOI: 10.1103/PhysRevLett.126.196402. URL: <https://link.aps.org/doi/10.1103/PhysRevLett.126.196402>.
- [49] L. B. Shao et al. “Gauge-Field Extended $k \cdot p$ Method and Novel Topological Phases”. In: *Phys. Rev. Lett.* 127 (7 Aug. 2021), p. 076401. DOI: 10.1103/PhysRevLett.127.076401. URL: <https://link.aps.org/doi/10.1103/PhysRevLett.127.076401>.
- [50] Haoran Xue et al. “Projectively Enriched Symmetry and Topology in Acoustic Crystals”. In: *Phys. Rev. Lett.* 128 (11 Mar. 2022), p. 116802. DOI: 10.1103/PhysRevLett.128.116802. URL: <https://link.aps.org/doi/10.1103/PhysRevLett.128.116802>.
- [51] Tianzi Li et al. “Acoustic Möbius Insulators from Projective Symmetry”. In: *Phys. Rev. Lett.* 128 (11 Mar. 2022), p. 116803. DOI: 10.1103/PhysRevLett.128.116803. URL: <https://link.aps.org/doi/10.1103/PhysRevLett.128.116803>.
- [52] Z. Y. Chen, Shengyuan A. Yang, and Y. X. Zhao. “Brillouin Klein bottle from artificial gauge fields”. In: *Nature Communications* 13.2215 (Apr. 2022). DOI: 10.1038/s41467-022-29953-7.
- [53] Yu-Liang Tao et al. “Higher-order Klein bottle topological insulator in three-dimensional acoustic crystals”. In: *Phys. Rev. B* 109 (13 Apr. 2024), p. 134107. DOI: 10.1103/PhysRevB.109.134107. URL: <https://link.aps.org/doi/10.1103/PhysRevB.109.134107>.
- [54] Zhenxiao Zhu et al. “Brillouin Klein space and half-turn space in three-dimensional acoustic crystals”. In: *Science Bulletin* 69.13 (2024), pp. 2050–2058. ISSN: 2095-9273. DOI: <https://doi.org/10.1016/j.scib.2024.05.003>. URL: <https://www.sciencedirect.com/science/article/pii/S2095927324003372>.
- [55] Jinbing Hu, Songlin Zhuang, and Yi Yang. “Higher-Order Topological Insulators via Momentum-Space Nonsymmorphic Symmetries”. In: *Phys. Rev. Lett.* 132 (21 May 2024), p. 213801. DOI: 10.1103/PhysRevLett.132.213801. URL: <https://link.aps.org/doi/10.1103/PhysRevLett.132.213801>.
- [56] Yanqiu Wang et al. *Chess-board Acoustic Crystals with Momentum-space Non-symmorphic Symmetries*. 2023. arXiv: 2305.07174 [cond-mat.mes-hall]. URL: <https://arxiv.org/abs/2305.07174>.
- [57] Yu-Liang Tao, Jiong-Hao Wang, and Yong Xu. *Quadrupole Insulator without Corner States in the Energy Spectrum*. 2023. arXiv: 2307.00486 [cond-mat.mes-hall]. URL: <https://arxiv.org/abs/2307.00486>.
- [58] J. Lukas K. König et al. *Exceptional Topology on Nonorientable Manifolds*. 2025. arXiv: 2503.04889 [cond-mat.mes-hall]. URL: <https://arxiv.org/abs/2503.04889>.

- [59] George William Whitehead. *Elements of Homotopy Theory*. Graduate Texts in Mathematics. Springer, 2012. ISBN: 978-1-4612-6320-3. DOI: 10.1007/9781-4612-6318-0.
- [60] Loring W. Tu. *Introductory Lectures on Equivariant Cohomology: (AMS-204)*. Princeton University Press, Mar. 2020. ISBN: 9780691191751. DOI: 10.23943/princeton/9780691191751.001.0001. URL: <https://doi.org/10.23943/princeton/9780691191751.001.0001>.
- [61] Graeme Segal. “Equivariant K-theory”. In: *Publications Mathématiques de l'IHÉS* 34 (Jan. 1968), pp. 129–151. DOI: 10.1007/BF02684593.
- [62] Glen E. Bredon. *Topology and geometry*. 139. Springer International Publishing, 1993. ISBN: 978-1-4419-3103-0. DOI: 10.1007/978-1-4757-6848-0.
- [63] Raoul Bott and Loring W. Tu. *Differential Forms in Algebraic Topology*. 82. New York, NY: Springer Science+Business Media New York, 1982. ISBN: 978-1-4419-2815-3. DOI: 10.1007/978-1-4757-3951-0.